SUPERCONDUCTIVITY AS A STRUCTURAL CHARACTERIZATION TOOL IN AMORPHOUS MATERIALS

Thesis by

Bruce Montgomery Clemens

In Partial Fulfillment of the Requirements

for the Degree of

Doctor of Philosophy

California Institute of Technology

Pasadena, California

1982

(Submitted September 22, 1982)

TO MY PARENTS

ACKNOWLEDGEMENTS

I would like to acknowledge the support and encouragement of my adviser, Professor William Johnson, whom I admire as a scientist and a person. I feel I was very lucky to have as an adviser a person who possesses a great deal of knowledge and a joy in sharing it with others. I would like to thank Professor Johnson for introducing me to the field of superconductivity and I would like to thank both Professor Johnson and Professor Pol Duwez for introducing me to the field of amorphous and metastable materials.

I would like to thank Dr. Michael Tenhover for his assistance and interest in this work. For technical assistance I would like to acknowledge the friendly support of Concetto Geremia, Angela Bressan, Sumio Kotake, Joe Wysocki, Hin-Wing Kui, and the staff of the Bitter Magnet Lab. I would like to thank Robert Schulz for his help in resistivity measurements and computerization of the critical current apparatus. I am grateful to Madhav Mehra for a fruitful collaboration in the study of sputtered films and I wish to thank Dr. Marc-Aurele Nicolet, Bai Xien Liu and Rolly Gaboraiud for their part in the collaborative study of ion beam mixed materials.

I would like to acknowledge Dr. Randall Feenstra, Reuben Collins, Stuart Hopkins, Dr. Konrad Samwer, Dr. Arthur Williams and Lowell Hazelton for helpful conversations.

I am grateful to Carolyn Meredith and Vere Snell for their cheerful and efficient typing of this manuscript.

Most of all I wish to thank Susan, my wife, for her faith and support. Those who know me realize that she was responsible for a turning point in my life and career as a scientist.

For financial support I acknowledge the Department of Energy and the International Business Machine Corporation.

ABSTRACT

This thesis presents the use of superconductivity as a structural probe for studying amorphous and metastable materials. The characteristics of the superconducting state which facilitate its use as a probe are explained, followed by a description of some of the properties of the materials studied. The superconducting measurements performed were critical current, transition temperature and upper critical field. Materials prepared by rapid quench from the melt, sputter deposition and ion beam mixing were studied. The critical current measurements performed on liquid quenched materials reflect three pinning mechanisms. Crystalline inclusions in otherwise amorphous $(Mo_{0.6}Ru_{0.4})_{80}Si_{10}B_{10}$ produced a dramatic increase in critical current. The pinning in purely amorphous $(Mo_{0.6}Ru_{0.4})_{82}B_{18}$ was shown to be affected by pinning by surface roughness on the sample edges. This contribution can be eliminated by a proper sample geometry and electropolish treatment. The bulk pinning in purely amorphous $(Mo_{0.6}Ru_{0.4})_{82}B_{18}$ was shown to first decrease and then increase as a function of annealing time. This reflects the disappearance of quenched in inhomogeneous strains and excess volume defects followed by the growth of an inhomogeneity such as compositional phase segregation during an anneal. The upper critical field was measured for liquid quenched $(Mo_{0.6}Ru_{0.4})_{1-x}B_x$ for x = 0.12, 0.18 and 0.22 both before and after an anneal. The annealed samples exhibited greater transition widths and more curvature in the $H_{c_2}(T)$

curves than the unannealed samples which are evidence for a growth of inhomogeneities upon annealing. Measurements on sputter deposited $(Mo_{0.6}Ru_{0.4})_{82}B_{18}$ were performed on samples sputtered in low (5 μm) and high (75 μm) Ar pressure. The material sputtered in low Ar pressure had a greater drop in T_c than the liquid quenched material and a pinning profile which exhibited a peak near H_{c_2}. The sample sputtered in high Ar pressure was very inhomogeneous as evidenced by transition width and flux pinning force profile. Measurements were performed on ion beam mixed $Mo_{55}Ru_{45}$. The structure consisted of an amorphous matrix with crystalline inclusions. The pinning profile was characteristic of a strong pinning mechanism. The pinning force decreased then increased as a function of ion beam dose. This reflects the destruction of the remnants of the original structure followed by the formation of an inhomogeneity such as σ-MoRu or Xe gas bubbles during ion beam irradiation.

TABLE OF CONTENTS

LIST OF TABLES

LIST OF FIGURES

I. Introduction

A. Superconductivity as a Materials Structural Probe

Amorphous materials have presented both the theorist and experimentalist with a challenge. The theorists have responded to the lack of long range order with new formalisms for calculating properties of solids which rely on local atomic environments. [1,2] The experimentalist finds that structural probes, such as x-rays and neutrons, supply only information which is an average of possible atomic configurations rather than the precise structural information obtained by the crystallographer. [3] Interpretation of transport properties is complicated by the lack of well defined Brillouin zones and Fermi surfaces. The effects of defects and inhomogeneities are difficult to study when the concept of what constitutes a defect or inhomogeneity is not clear.

This thesis presents the use of superconductivity as a probe to characterize the structural state of amorphous materials. The superconducting state samples the material properties with a characteristic sampling dimension equal to roughly the size of a Cooper pair. Thus the effects of the introduction of defects and inhomogeneities of sizes comparable to this length should be observable. The properties studied in this investigation are transition temperature, upper critical field and critical current. Of these three, critical current measurements have been of the most value in this study. As explained in later chapters these measurements make use of the mixed or Schubnikov

state of the superconductor to directly observe the presence of inhomogeneities.

Several problems dealing with amorphous materials have been addressed in this work. The effects of the presence of crystalline inclusions, the effect of roughness of the sample edges and the effect of thermal anneals have all been studied in liquid quenched amorphous materials. Evidence which suggests a segregation into two amorphous phases as a precursor to crystallization is presented. In addition to amorphous materials prepared by liquid quenching, samples made by sputtering and ion beam mixing have also been studied to observe the effects of different preparation techniques.

The results presented within this study show that superconductivity can be a valuable tool in the study of the metallurgical state of amorphous materials. Several problems have been successfully addressed, and we have obtained structural information which is difficult or impossible to obtain by other methods.

B. Historical Background

Although the science of amorphous metals is new and developing, metals which were most probably amorphous were fabricated by chemical deposition as early as 1845.[4] Early workers in the field of electroless deposition concentrated on mechanical properties, but in 1950 x-ray diffraction was used to demonstrate that a deposit of Ni-P was amorphous.[5] In 1954 Buckel and Hilsch[6] discovered that by

vacuum deposition on cryogenically cooled substrates, thin films of amorphous simple metals could be produced. While measuring resistivity they discovered that amorphous films of Bi and Ga were superconducting. The first bulk amorphous metals were produced by Duwez et al in 1960 [7] by rapidly quenching from the melt an alloy of composition $Au_{80}Si_{20}$. Since that time a rich variety of amorphous alloys has been prepared by the rapid quenching technique.

Following the discovery of superconducting amorphous Bi and Ga, Buckel and Hilsch produced a variety of superconducting amorphous non-transition metals. The first work in cryoquenched transition metal films was done by Strongin et al. [8] This was followed by a systematic investigation of amorphous transition metal alloys formed by evaporation onto cryogenic substrates reported by Collver and Hammond. [9] This investigation resulted in amorphous superconductors which are stable to temperatures up to several hundred degrees Kelvin. The first liquid quenched amorphous superconductor reported was $La_{76}Au_{24}$ in 1975 by Johnson and Poon. [10] In the past 10 or so years research in the field of amorphous superconductors has experienced considerable growth. The activity in this field is stimulated by the interesting and unique properties of amorphous superconductors which have both scientific importance and possible practical application. Aspects of the theory of superconductivity relevant to this work will be covered in the following section with emphasis on the properties of amorphous superconductors.

II. Theoretical Background

A. Superconductivity

1. Microscopic Theory of Superconductors

a. General Theory

Superconductivity was discovered in 1911 by H. Kamerling-Onnes.[11] He found that the electrical resistance of some metals dropped to zero at a temperature, T_c, characteristic of the material. In 1933, Meissner and Ochenfeld [12] discovered that a superconductor will completely expel flux at fields up to a critical field H_c at which point the superconducting state is destroyed. It was not until 1957 that Bardeen, Cooper and Schrieffer (BCS) [13] presented a microscopic theory which successfully explained superconductivity. The details of BCS theory are outside the scope of this treatment but some understanding can be gained from a rather cursory examination of the aspects of BCS theory which are related to material properties. The basis for this theory is to represent the conduction electrons as a nearly free electron gas where the electrons interact in a phonon mediated attractive potential. [14] In the presence of any attractive interaction, the electrons at the Fermi surface are unstable against the formation of electron pairs. Under this unstability the electrons condense to a multiparticle state known as the BCS ground state. Fermion quasiparticles excitations can be created with an energy greater than some minimum excitation energy Δ. Thus there exists an energy gap in the excitation spectrum. The critical temperature (T_c) is the temperature

where the gap ($\Delta(T)$) goes to zero. Here the excitation spectrum becomes the same as in the normal state. The BCS theory expression for T_c is

$$T_c = 1.14 \langle\omega\rangle e^{-1/\lambda}$$

where λ is the electron phonon coupling constant and $\langle\omega\rangle$ is an average phonon frequency. This expression is valid in the weak coupling limit ($\lambda << 1$). The BCS expression for λ is $\lambda = D(\varepsilon_F)V$ where $D(\varepsilon_F)$ is the electronic density of states at the Fermi surface and V is the matrix element for the indirect electron-electron attraction arising from the electron-phonon interaction. Eliashberg [15] has extended BCS theory to account for ω dependence of the electron-phonon matrix element ($\alpha(\omega)$) and the phonon frequency spectrum $F(\omega)$. McMillan [16] has used the Eliashberg theory to derive an expression for T_c which is valid in the strong coupling limit ($\lambda \sim 1$). He defines a new dimensionless coupling constant

$$\lambda = 2 \int \frac{d\omega \alpha^2(\omega)\ F(\omega)}{\omega}$$

and using the phonon spectrum for niobium derives an expression for T_c in terms of the coupling constant λ, the McMillan root mean square phonon frequency $\langle\omega^2\rangle$, and the screened coulomb pseudopotential μ^* ($\sim$0.13 for transition metals) yielding

$$T_c = \frac{\langle\omega^2\rangle^{\frac{1}{2}}}{1.45} \exp\frac{-1.04(1+\lambda)}{\lambda-\mu^*(1+0.62\lambda)}$$

The McMillan RMS phonon frequency is defined by

$$\langle\omega^2\rangle = \frac{\int \alpha^2(\omega)\, F(\omega)\, dw}{\int \frac{\alpha^2(\omega)\, F(\omega)\omega\, dw}{\omega}}$$

and McMillan has shown that λ can be rewritten as

$$\lambda = \frac{D(\varepsilon_F)\, \langle g^2\rangle}{M\, \langle\omega^2\rangle}$$

where $\langle g^2\rangle$ is a squared electron ion matrix element averaged over the Fermi surface and M is the ionic mass.

Two further points should be mentioned before moving on. First, the size of a Cooper pair can be roughly estimated from a simple uncertainty argument. The electrons involved in pairing are on the Fermi surface and travel at a group velocity equal to the Fermi velocity, v_f. Thus in the lifetime (τ) of a Cooper pair they travel a distance $v_f\tau$. If we equate this distance to the diameter (ξ) of a Cooper pair, and estimate the lifetime from an uncertainty principal argument then we find $\xi_o = \frac{\hbar v_f}{\Delta}$. This differs by a factor of $\frac{1}{\pi}$ from the BCS result, which is $\xi_o = \frac{\hbar v_f}{\pi\Delta}$.

Secondly, the energy density difference between the superconducting and normal states can be found from thermodynamic considerations to be $H_c^2/8\pi$ [14] where H_c is the thermodynamic critical field. If we imagine creating a gap in the density of states at the Fermi surface then we

must push the electron states out of the gap in forming the superconducting state. The number of electrons in the gap is roughly $D(\varepsilon_f)$ and the electrons must be pushed an energy $\frac{1}{2}\Delta$ in either direction. Thus we estimate the energy density required to be $\frac{1}{2}\Delta^2 D(\varepsilon_f)$ yielding the relationship $\frac{1}{2}\Delta^2 D(\varepsilon_f) = \frac{H_c^2}{8\pi}$, which is precisely the BCS result.

B. Microscopic Theory Applied to Amorphous Superconductors

The task of applying the microscopic theory of superconductivity to amorphous materials is complicated by their lack of long range order. This effects the electronic states and the vibrational modes. However, a formulism for defining the microscopic parameters involved in the McMillan equation for T_c (hereforth referred to as the McMillan equation) has been outlined by Johnson. [17] The free electron metals are well described by a simple Jellium model which involves pseudopotential theory for the electron phonon interaction. These materials often tend to be strong coupling ($\lambda > 1$) reflecting the enhancement of low frequency phonon modes due to disorder. [18]

Amorphous transition metal superconducting behavior is dominated by the large contribution of the d electrons to the density of states ($D(\varepsilon_f)$). Thus the tight-binding approach is appropriate in this case. Varma and Dynes [19] have derived an approximate expression for λ; $\lambda = D(\varepsilon_f)W(1\pm S)$ where W is the width of the d band, S is the overlap of neighboring d orbitals and $1\pm S$ is the nonorthagonality factor. The

McMillan rootmean square phonon frequency is viewed as a characteristic phonon frequency and often $\theta_D/2$ (θ_D is the Debye temperature from low temperature specific heat measurements) is used in applying the McMillan equation. With the observed T_c one can then find λ which can be used in testing the theory. Johnson [17] has found that the Varma Dynes approach accounts reasonably well for the systematics of T_c in these materials.

2. Ginsburg-Landau Theory

a. General Theory

The behavior of a superconductor in the presence of an external field or transport current can be described by the Ginsburg-Landau theory.[14,20] This is a general phenomenological theory for describing higher order phase transitions. Abrikosov and Gorkov [21] have shown that this theory can be derived from the microscopic superconducting theory, thus putting G-L theory on sound fundamental footing as well as allowing the calculation of G-L theory parameters in terms of the microscopic model. The basis for this theory is a free energy expansion in terms of even powers of an order parameter ψ and its gradient

$$f = f_n + \alpha|\psi|^2 + \beta|\psi|^4 + \cdots + \gamma|\nabla\psi|^2 + \cdots$$

where f_n = free energy density of normal phase.

The crucial breakthrough for the application of this theory to a superconductor in a field occurred when Landau postulated that ψ might be viewed as a superparticle wave function with $|\psi|^2$ being the density

of supercurrent carriers. The supercurrent carrier would have mass M^* and charge e^*. The gradient operator in the free energy expansion must be replaced by the quantum mechanical gradient operator, $(\frac{\hbar}{i}\vec{\nabla} - \frac{e^*}{c}\vec{A})$. Where $\vec{A}$ = the vector potential. Thus the free energy density becomes

$$f = f_n + \alpha|\psi|^2 + \frac{\beta}{2}|\psi|^4 + \frac{1}{2M^*}\left|\left(\frac{\hbar}{i}\vec{\nabla} \frac{e^*}{c} \vec{A}\right)\psi\right|^2 + \frac{h^2}{\gamma\pi}$$

where h is the local field. The next step is to minimize the free energy in terms of ψ and $\vec{A}$. This results in the celebrated Ginsburg-Landau equations

$$1) \quad \alpha\psi + \beta|\psi|^2\psi + \frac{1}{2M^*}\left(\frac{\hbar}{i}\vec{\nabla} - \frac{e^*}{c} \vec{A}\right)^2\psi = 0$$

$$2) \quad J = \frac{c}{4\pi} \text{ Curl } \vec{h} = \frac{e^*\hbar}{2M^* i}(\psi^*\vec{\nabla}\psi - \psi\vec{\nabla}\psi^*) - \frac{e^{*2}}{M^* c} \psi^*\psi\vec{A}$$

These are in general non-linear differential equations with no analytical solution. They can be shown to have simple solutions in limiting cases which can illuminate physical quantities which continue to exist in the general case. Several of these limiting cases will be examined.

In the absence of gradients and fields we have $\alpha\psi + \beta|\psi|^2\psi = 0$ which gives $|\psi|^2 = -\alpha/\beta$. In this case the order parameter is constant

in space and is conventionally denoted as ψ_∞. The energy difference between the superconducting and normal states is $-\alpha^2/\beta$ which can be equated to the expression for condensation energy in BCS theory. The temperature dependence of ψ_∞ can be found from a Taylor expansion about T_c of the coefficients α and β. At T_c the system can first begin to lower its energy by having $\psi \neq 0$. Thus, as temperature is decreased below T_c, α must change sign from positive to negative. Thus, to first order in temperature $\alpha = \alpha'(T - T_c)$. The first order term for β is constant giving $|\psi_\infty|^2 = \frac{-\alpha'(T-T_c)}{\beta} \alpha\ 1-t$, $(t = T/T_c)$.

When we allow the order parameter to vary spatially the gradient terms must be included. A simple one-dimensional treatment can serve to demonstrate this behavior. Using a normalized wave function $f = \psi/\psi_\infty$ the first G-L equation becomes $\xi^2(T) \frac{d^2f}{dx^2} + f - f^3 = 0$ where $\xi^2(T) = \frac{\hbar^2}{2M^*|\alpha(T)|}$. $\xi(T)$ is the characteristic length over which the order parameter can vary. From our previous result we see that $\xi(T) \alpha (1-t)^{-1/2}$.

A second characteristic length can be found by examining the case where there exists no gradients in ψ but the vector potential is non-zero. The second G-L equation then yields $\vec{J} = \frac{-e^2}{Mc}|\psi|^2\vec{A}$. By applying Maxwell's equation and simple vector algebra we obtain $\nabla^2\vec{h} = \lambda^2\vec{h}$ where h is the local field ($\vec{\nabla} \times \vec{h} = \frac{4\pi}{c}\vec{J}$) and $\lambda^2 = \frac{Mc^2}{4\pi e^2 n}$. Thus, the characteristic length over which the local field can change is λ. This is known as the penetration depth.

By examination of the first G-L equation in the limit of small ψ we can find the highest applied field for which a superconducting state exists. We have $\frac{1}{\xi^2}\psi + (\frac{\nabla}{i} - \frac{2\pi}{\phi_o})^2\psi = 0$. Where $\phi_o = \frac{hc}{2e}$ is the fundamental flux quanta which will be discussed later. Making the substitution $\psi = e^{ik_y y} e^{ik_z} f(X)$ yields $f''(X) + \frac{2\pi H^2}{\phi_o}(X-X_o)f=(\frac{1}{\xi^2} - k_z^2)f$. This is the equation for harmonic oscillator with energy eigen values $(n - 1/2)\hbar\frac{2eH}{M^* c}$, thus, $\frac{1}{\xi^2} - k_z = (n + 1/2)\frac{2\pi H}{\phi_o}$. Solving for H gives $H = \frac{\xi_o}{2\pi(2n+1)}(\frac{1}{\xi^2} - k_z^2)$. This has its highest value when $n = 0$ and $k_z = 0$. This quantity, known as the upper critical field and denoted by H_{c_2} is given by $H_{c_2} = \frac{\phi_o}{2\pi\xi^2(T)}$. From earlier results we find $H_{c_2}(t) \alpha 1-t$. A more exact treatment based on the microscopic theory has been carried out by Maki [22] and Werthamer, Helfand and Hohenbeg [23] to find $H_{c_2}(t)$ at temperatures far from T_c. They have included effects such as paramagnetic limiting and spin orbit coupling. Paramagnetic limiting tends to decrease H_{c_2} due to the interaction of the electronic spins with the external field. The spins of the electrons involved with pairing tend to align with the field and thus the pair is broken. Spin orbit scattering tends to decrease the ability of an external field to align the spins and break the pairs. Results of their calculation for $H_{c_2}(t)$ at different values of the parameters α (paramagnetic limiting) and λ_{so} (spin orbit scattering) are shown in Figure 1.

The relationship between H_{c_2} and H_c can be found from G-L expressions covered previously to be $H_{c_2} = \sqrt{2}\frac{\lambda}{\xi}H_c$. Thus, if we have the

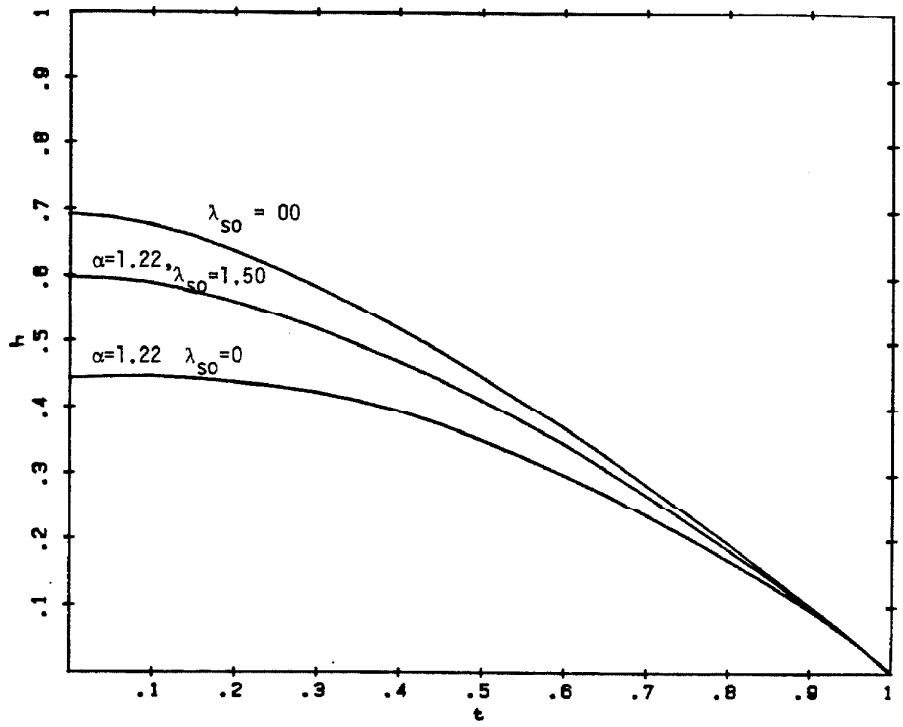

Figure 1. Results of the WHH[23] calculated for $h(t)=H_{c_2}(T)/[(T-T_c)\left.\frac{dH_{c_2}}{dT}\right|_{T_c}]$ for different values of the parameters λ_{so} (spin orbit coupling parameter) and α (paramagnetic limiting strength).

case where $\lambda > \sqrt{2}\,\xi$ then superconductivity can exist at fields higher than the thermodynamic critical field. This type of superconductor is known as a Type II superconductor. As explained in a later section, all amorphous superconductors are Type II.

The flux which enters a superconductor does so in units of ϕ_0, the fundamental flux quanta. This can be seen by looking at the second G-L equation. If we make the substitution $\psi = a(r)\, e^{i\gamma(\vec{r})}$ we find $\vec{J} = \frac{e^*}{m}|\psi|\,[\hbar\vec{\nabla}\gamma - \frac{e^*}{c}\vec{A}]$. However far away from penetrated flux, deep in the superconductor $\vec{J} = 0$ so $\hbar\vec{\nabla}\gamma = \frac{e^*}{c}\vec{A}$. By doing a line integral around the included flux and requiring ψ to be single valued, we find an expression for penetrated flux, $\phi = n\phi_0$.

Abrikosov [24] has shown that the energy of the interface between superconducting and normal regions is negative for Type II superconductors and positive for Type I superconductors. This is due to the fact that the domain wall energy is dominated by decrease in condensation energy loss in the normal region (length $\sim\xi$) near the interface in Type I whereas in the Type II it is dominated by the decrease in energy due to penetration of the field in the region (length $\sim \lambda$) near the interface. This results in the flux penetrating the Type II superconductor in lines each containing a single flux quanta. The result is a lattice of flux lines in the superconductor with an areal density given by $n = B/\phi_0$. This state is called the Schubnihov or mixed state.

The structure of an individual flux quanta is shown in Figure 2. [14] The flux line is characterized by two occurrences. The first is the

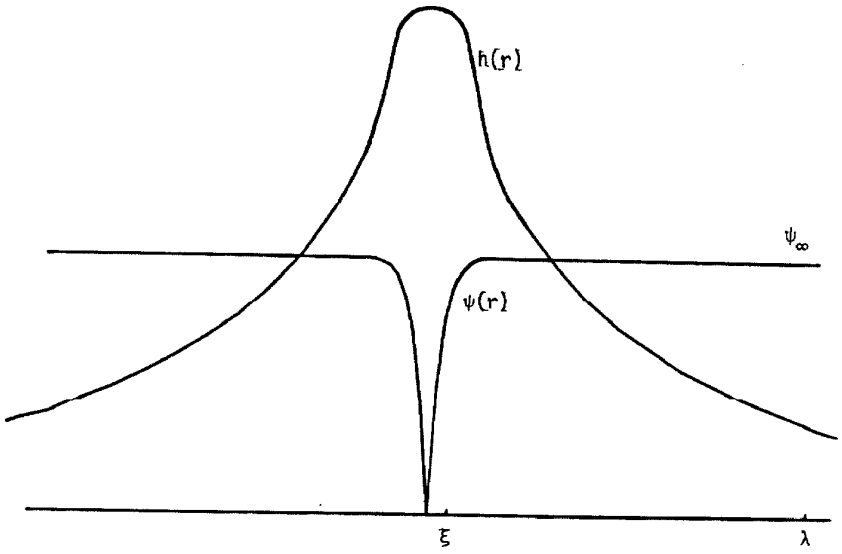

Figure 2. Reduced field $h(r)$ and order parameter $\psi(r)$ as a function of position near an isolated vortex in a material where $\lambda/\xi = 20.14$.

dip in the order parameter to a value of $\psi = 0$ at the center of the vortex. This occurs over a characteristic distance ξ and is sometimes modeled as a cylindrical core region with radius ξ which has $\psi = 0$. The second occurrence is the variation of the local magnetic field h from h = 0 far away from the vortex to some finite value at the vortex core. This variation occurs over a characteristic length λ. For the case shown in Figure 2 the ratio $\lambda/\xi = 20$.

The field at which flux first penetrates the superconductor is called the lower critical field and is denoted as H_{c_1}. This is related to the thermodynamic critical field by $H_{c_1} = \frac{H_c \xi}{2\lambda} \text{Ln} \frac{\lambda}{\xi}$. [14] At fields between H_{c_1} and H_{c_2} the superconductor will exist in the mixed state. There is perfect diamagnetism (Meisner effect) only up to H_{c_1} at which point the magnetic induction, B, ($B = H - 4\pi M$) becomes non-zero.

In the limit where $\lambda >> \xi$ the field associated with an isolated vortex can be found to be $h(r) = \frac{\phi_o}{2\pi\lambda^2} K_o(\frac{r}{\lambda})$ [14] where r is measured from the vortex center and K_o is a zero-order Hankel function of imaginary argument. At long distances this falls off as $e^{-r/\lambda}$. The vortex-vortex interaction energy (E) is given by $E = \frac{\phi_o^2}{8\pi^2\lambda^2} K_o(\frac{r_{12}}{\lambda})$. Where r_{12} is the distance between two vortices. The force between two vortices can be calculated by taking the derivative yielding the simple result $\vec{f}_2 = \vec{J}_1(r_2) \times \frac{\phi_o}{c}$ where f_2 is the force on vortex 2 caused by vortex 1, $J_1(r_2)$ is the current density of vortex 1 at the position of vortex 2. By generalizing to an array of vortex lines we find $\vec{f} = \vec{J} \times \frac{\phi_o}{c}$ where $\vec{J}$ is now the total

current from the entire vortex lattice. Due to this interaction, the vortices seek an equilibrium position with respect to each other in a symmetric array. The lowest energy array for a homogeneous and isotropic material is a triangular lattice. The flux line lattice constant (a_o) will be given by $a_o = 1.075(\frac{\phi_o}{B})^{1/2}$.

b. Amorphous Materials

In amorphous materials each atom acts as an electron scattering site. This results in a very short electronic mean free path as can be deduced from resistivity measurements. This allows us to work in what is known as the "dirty limit" when evaluating the parameters in G-L theory. To demonstrate this, let us examine the effect of scattering on the size of a Cooper pair. As mentioned in the section of this thesis which dealt with BCS theory, the size of a Cooper pair is the distance the electrons involved in pairing travel during the lifetime of a Cooper pair. If the electron is scattered several times during the lifetime of the pairing, then the path traveled is described by a random walk process and the total distance traveled is given by $d = \ell_e\sqrt{N}$ where ℓ_e is the electronic mean free path and N is the number of steps taken which is just the ratio of the Cooper pair lifetime to the electron scattering time ℓ_e/v_f. This gives $\xi = \sqrt{\xi_o \ell_e}$, or that the coherence length in the presence of scattering is just the geometric mean of the "clean limit" coherence length and the electron mean free path. The result of a more accurate evaluation of the "dirty limit" G-L coherence length from BCS theory

gives $\xi(t) = 0.855 \frac{\sqrt{\xi_o \ell e}}{(1-t)^{1/2}}$, [14]

The penetration depth however is increased by electronic scattering since this decreases their effectiveness in screening the field. The result for the "dirty limit" penetration depth is

$\lambda(t) = \lambda_L(t)(\frac{\xi_o}{1.33\ell e})^{1/2}$ [14] where $\lambda_L = \frac{Mc^2}{4\pi e^2 n}$, The increase in the penetration depth λ, coupled with the decrease in the coherence length ξ means that their ratio $(\lambda/\xi) \equiv \kappa$ is very large for strong scattering materials. Amorphous materials have the highest κ's reported for any known superconducting materials with values ranging from 50 to 100. Therefore, amorphous materials are extreme Type II superconductors.

One of the effects of a large κ is a high H_{c_2} relative to H_c and thus a higher H_{c_2} for a given gap (recall $f_s - f_n = \frac{H_c^2}{8\pi} = \frac{1}{2}\Delta^2 D(\varepsilon_f)$). Another effect is that H_{c_1} is very small in comparison to H_{c_2} since $H_{c_2}/H_{c_1} = \frac{2\kappa^2}{\ell n \kappa} \sim 1000\text{-}4000$ in amorphous materials. The magnitude of the magnetization is at most $H_c/4\pi$ and thus magnetization effects are negligible at fields comparable to H_{c_2} so we take B = H.

3. Flux Pinning

In a material where the superconducting properties are homogeneous the flux lines will arrange themselves into a stationary perfect triangular lattice. If an external current density ($\vec{J}$) is applied, the current in the vortices will interact with the external current density to produce a force density on the flux line lattice given by $F = \vec{J} \times \vec{H}$. This will cause a motion of the flux line lattice in the direction of the force which is perpendicular to the current. A dissipative voltage, V, along the direction of the current will be due to the velocity v_ϕ of the flux line lattice given by $E = -\nabla V = -v_\phi \times H/c$. Kim et al[25] originally suggested that the flux lines dissipate energy as they move and thus experience a viscous drag. There will then be a viscous force, F_v given by $v_\phi \eta$, where η is a viscous drag coefficient, which counters the Lorentz force. This will produce a linear I-V curve with resistivity ρ given by $\rho = B\phi_o/c\eta$. Experimentally it is found that $\rho = \rho_n H/H_{c_2}$ where ρ_n the normal state resistivity.

In actual materials, the superconducting properties can vary spatially which results in the energy of the flux line lattice being a function of the position of the flux lines. The Lorentz force must then push the flux lines through a potential which varies in space. This is called the pinning potential well. There will be no flux line motion and thus no dissipative voltage along the direction of the current until the Lorentz force exceeds the forces associated with the

pinning potential. The critical current density, J_c, is defined as the current at a given field which produces a Lorentz force sufficient to move the flux line lattice as a whole and produce a dissipative voltage. At current densities greater than J_c the flux lines will flow and the I-V curve will be linear in this region. The sample is no longer strictly speaking superconducting.

The problem of calculating the flux pinning force density can be broken into two parts. The first part consists in calculating the fundamental flux line-defect interaction force f_p for an isolated flux line. The second part consists of summing the individual flux line-defect forces to obtain the total force density. In carrying out the sum the statistical nature of the flux line-defect forces due to the distribution of defects in space and pinning strength, and the flux line-flux-line interactions must be taken into account. The total problem is formidable and it is not clear that either part of the problem has been successfully completed. One approach has been to formulate an expression for F_p of the form $F_p = CH_{c_2}{}^n f(h)$ where C is a constant independent of H and T, h is the reduced field H/H_{c_2} and n and f(h) are characteristic of the pinning mechanism operating in the superconductor.[26,27]

The individual flux line-defect interaction force is in general dependent on the size and shape of the defect as well as the superconducting properties of the defect relative to the host material. In the simple case of a large sphere with diameter d of normal material the energy of the flux line can be lowered by situating the flux

line so as to pass through this region since the local field no longer must drive the core region normal. The amount that the energy is lowered is the condensation energy density times the volume of interaction. This results in $f_p \alpha (1-h)$. For a line or plane defect the number of flux lines which can interact with a given pinning center goes as $1/a_o$ where a_o is the flux line lattice spacing this gives $f \alpha h^{1/2}(1-h)$. [27] A more general treatment is possible by working with the Ginsburg-Landau free energy and looking at the change in free energy associated with spatial variations in the parameters α and β. Huebner[28] has carried over this type of treatment for small pinning centers possessing an H_{c_2} different from the matrix and also found $f_p \alpha h^{1/2}(1-h)$. For the purposes of this thesis we have used both of these forms for the individual flux line pinning center interaction in attempting to account for experimental observations. Due to the uncertainties in the summation problem covered in the next section it is not always clear which one is applicable in the case of amorphous materials or in fact if either one is correct.

The problem of summation of the individual flux line-pinning center interactions can be approached from several different viewpoints. There are, in particular, three most popular approaches. The statistical model of Labusch [29], the dynamic pinning model of Yamafugi and Eri [30] and Kramer [26], and the collective pinning approach of Laukin and Ovchivnikov [31], Campbell and Everts [27] have

shown that the first two yield the same results so we will concentrate our discussion of this problem in terms of two models, the dynamic pinning model and the collective pinning model.

In most critical current measurement techniques, one observes a finite voltage along the direction of current. This means that the flux lines are moving through the pinning centers. The dynamic pinning model takes this motion into account and finds the pinning force F_p from the pinning power loss density $F_p\langle V\rangle$ where $\langle V\rangle$ is the average flux line velocity. The pinning power loss is dissipated in the flux line lattice by local excursions in the flux line velocity from its average value. This power loss can be identified as the rate at which elastic energy is stored in the flux line lattice. Thus, we can approximate the power loss density by $F_p\langle V\rangle = 2\rho E_s\langle V\rangle/a_o$ where ρ is the density of pinning centers, E_s is the static energy of a flux line-pinning center interaction and $\langle V\rangle/a_o$ is the plucking frequency or average rate at which a pinning center interacts with the flux line lattice. The most obvious approach to finding E_s is to use a Hooke's law approximation and write $E_s = 1/2\frac{f_p^2}{c}$ where c is the elastic constant for the flux line lattice. Thus, the pinning force density is found to be $F_p = \frac{f_p^2}{ca_o}$.

The elastic constant in this expression is an effective elastic constant for the flux line lattice. The proper modulus chosen in the case of any given pinning mechanism depends upon how elastic energy is stored in the flux line lattice (i.e., in shear, beading compression, etc.). Several authors [26,27,29] have addressed the

problem of which lattice constant to use in different situations. In general the results are in terms of combinations of the three flux line lattice constants; c_{11}-compression modulus, c_{44}-bending modulus and c_{66}-shear modulus. Labusch [29] has found three regions of flux line lattice deformation energy behavior

1) $c = \frac{1}{\sqrt{c_{11}c_{44}}} + \frac{1}{\sqrt{c_{66}c_{44}}}$ In this region the response of the flux line lattice is determined by the lattice rigidity so this is called the lattice approximation,

2) $c = \frac{1}{\sqrt{c_{11}c_{44}}} + \frac{\pi}{\sqrt{\alpha c_{44}}}$ In this region c_{66} plays no part in the lattice response so this is termed the fluid approximation. (α is a parameter characterizing the strength of the pinning potential.)

3) $c = \frac{1}{\sqrt{\alpha c_{44}}}$ This is the single fluxoid approximation since the bending modulus is independent of flux-line-flux line interactions.

Near H_{c_1} the single fluxoid interaction will be applicable. At greater fields the fluid approximation will be reached and at still greater fields the lattice approximation is appropriate. The exact fields where the crossover takes place is dependent upon the strength of the pinning mechanism, the weaker the pinning mechanism the smaller region in the field where the single fluxoid and fluid

approximations are valid. Labusch [29] concludes that the lattice approximation is the most important for application to actual superconductors.

Kramer [26] has suggested that Labusch's lattice approximation is valid for point pins but that for line pins the effective modulus becomes c_{66}. Pearls [32] has shown that in the region near the surface, the flux line-flux line interaction goes as 1/r at long distances as compared with the exponentially decreasing interaction in the bulk. This tends to increase the compressibility and decrease the shear modulus of the flux line lattice. This decrease in the shear modulus led Kramer and Das Gupza,[33] and Das Gupza and Kramer [34] to postulate that the elastic energy of deformation of the flux line lattice near the surface is dominated by the bending modulus.

The relative strength and field dependences of the flux line lattice elastic constants have been calculated by Brandt. [35] He has found $c_{66} << c_{11}$ so that the effective modulus for Labusch's lattice approximation becomes $c \approx \sqrt{c_{44}c_{66}}$. He found that the shear modulus was well approximated by an analytical form for high κ, $c_{66} = \frac{H_{c_2}^2(t)}{4\pi} \frac{K}{K_2^2} h(1-0.29h)\ (1-h)^2$; $(h = H/H_{c_2})$. Campbell and Evetts [27] have found that $c_{44} = BH = H^2$.

The flux pinning profile $F_p(h)/F_{p\ max}$ for the dynamic pinning model can now be calculated. From the results above we see that $F_p/F_{pm} \alpha h^m(1-h)^n\ (1-0.29h)^p$ with m, n, and p reflecting the form for f_p and the particular effective lattice constant used. The reduced

field at which the maximum occurs can be easily calculated. Table 1 summarizes the results for several possible cases. Note that some of the possible cases diverge at low h. This behavior is obviously non-physical and will be corrected by a modification of the theory. Figure 3 shows the pinning profile for the remaining cases.

Kramer [26] has suggested that when pins become very strong the pins do not break but the lattice shears around the strongly pinned lines. The elastic energy stored in this case is proportional to c_{66} leading to $F_s \alpha h(1-h)^2 (1-.3h)$, where F_s is the shearing force or the force required to shear the flux line lattice. The actual pinning force measured will be the smaller of the pin breaking or pin shearing. Pinning profiles generated by this model will have a sharp peak at a reduced field which is a function of the relative strengths of pin breaking and pin shearing. This peak can be rounded off by assuming a distribution of pinning strengths. Figure 4 shows a pinning profile generated by a model which takes $c = \sqrt{c_{44}c_{66}}$ and $f_p \alpha (1-h)$ and has the pin breaking to pin shearing strength such that $h_p = 0.11$. The results of choosing several different distributions are shown.

Larkin and Ovchinnikov [31] have presented a theory in which the pinning centers act in a collective manner to produce a pinning force density. This type of pinning should occur when a superconductor has a large number of randomly arranged weak pinning centers. This causes a breakdown of the long range order in the flux line lattice. Within a volume V_c there is a coherent lattice and the pinning forces acting

Case	Elastic Constant	f_p	F_p
1	$\sqrt{C_{44}C_{66}}$	$h^{1/2}(1-h)$	$(1-h)(1-0.29h)^{-1/2}$
2	$\sqrt{C_{44}C_{66}}$	$(1-h)$	$h^{-1}(1-h)(1-0.29h)^{-1/2}$
3	$\sqrt{\alpha C_{44}}$	$h^{1/2}(1-h)$	$h^{1/2}(1-h)^2$
4	$\sqrt{\alpha C_{44}}$	$(1-h)$	$h^{-1/2}(1-h)^2$
5	C_{44}	$h^{1/2}(1-h)$	$h^{-1/2}(1-h)^2$
6	C_{44}	$(1-h)$	$h^{-3/2}(1-h)^2$
7	C_{66}	$h^{1/2}(1-h)$	$h^{1/2}(1-0.29h)^{-1}$
8	C_{66}	$(1-h)$	$h^{-1/2}(1-0.29h)^{-1}$

TABLE 1. Pinning force field dependence for the various cases in the dynamic pinning model.

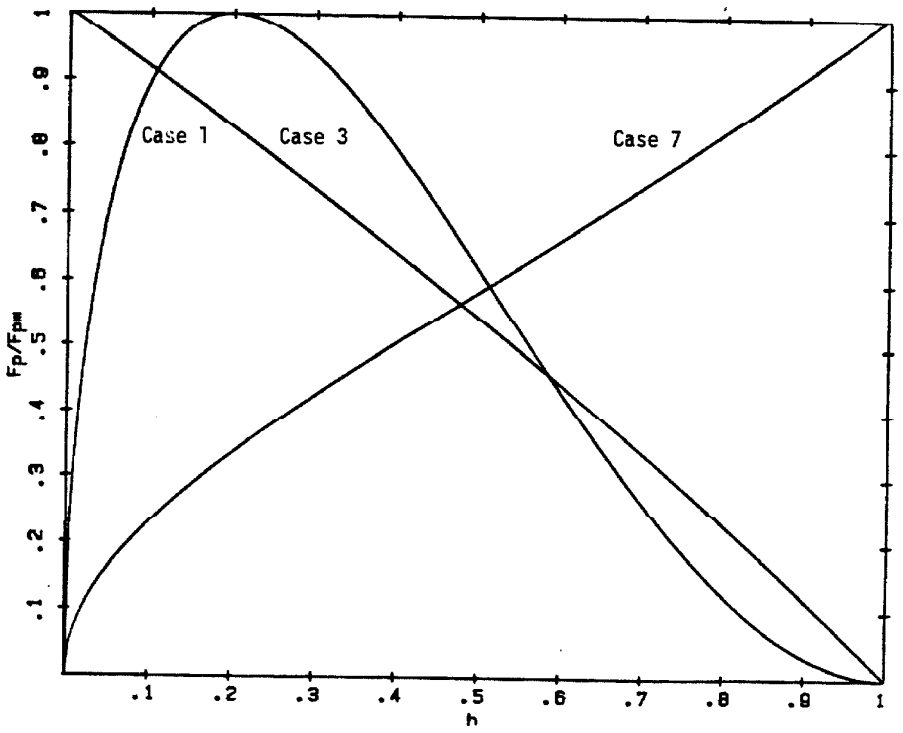

Figure 3. Pinning profiles for dynamic pinning model in non-diverging cases. Case numbers refer to Table 1.

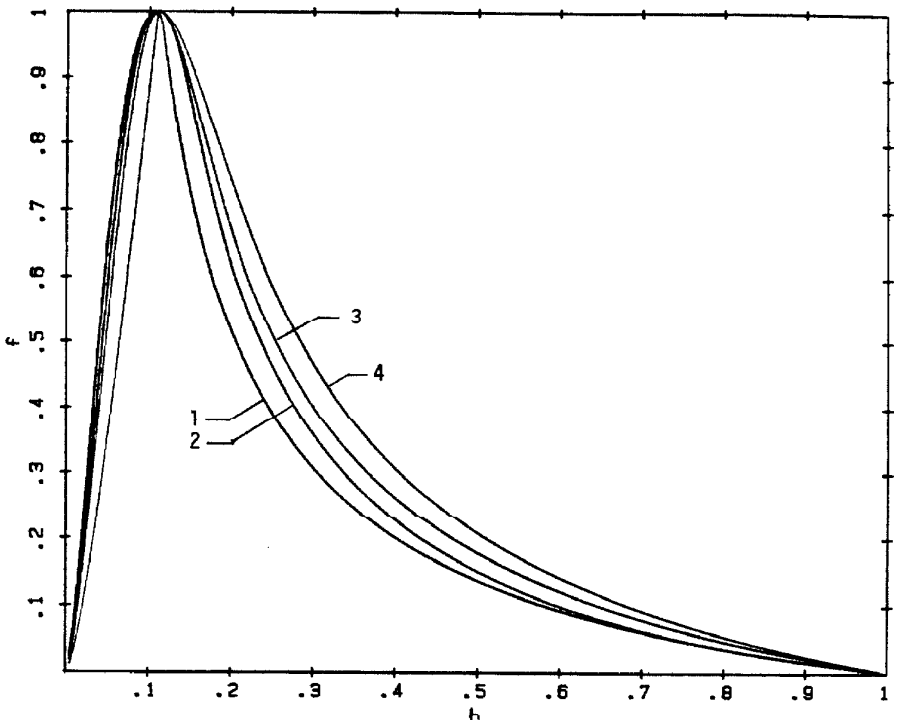

Figure 4. Pinning profiles generated by pin shearing model described in text. The numbers on graph refer to distributions of pin strength (k) in the following manner:

1. Point $\rho(k) = \delta(\langle k \rangle)$

2. Gaussian $\rho(k) = \frac{2}{\pi\langle k \rangle} e^{\frac{1}{\pi}(k/\langle k \rangle)^2}$

3. Poisson $\rho(k) = \frac{1}{\langle k \rangle} e^{-(k/\langle k \rangle)}$

4. Square Root $\rho(k) = \frac{1}{2\langle k \rangle} e^{-k/\langle k \rangle)^{1/2}}$

on either side of the pinning center compensate each other and the maximum pinning force is equal to $f_p N^{1/2}$ where N is the number of pinning centers in the volume V_c. The pinning force density is then $F_p = \frac{fN^{1/2}}{V_c} = f\left(\frac{n}{V_c}\right)^{1/2}$, where n is the density of pinning centers. The volume V_c can be found from a simple energetic argument. The dimension of V_c in any direction is taken to be the distances from a given flux line to where the flux lines are displaced from their unstressed position a distance a_o. Then one can write the free energy in terms of the elastic strain energy and the pinning interaction energy. Minimizing this quantity leads to equations for R_c, L_c, and V_c, where R_c is the dimension of V_c transverse to the field and L_c is the dimension of V_c along the field. The resulting expression for V_c is

$$V_c = \frac{256\ a^2\ c_{44}^2 c_{66}^4}{n^3 f^6}$$

This results in an expression for F_p which is

$$F_p = \frac{n^2 f^4}{16 a_o^3\ c_{44} c_{66}^2}$$

As the pinning strengths increase the transverse dimension, R_c of the coherent volume will decrease to its minimum value a_o. The pinning force will then be given by

$$F_p = \frac{f^{4/3} n^{2/3}}{4^{1/3}\ a_o^{5/3}\ c_{44}^{1/3}}$$

The pinning profiles generated by this model have a variety of shapes depending upon the crossover point between the regions. Several typical profiles generated by this model are shown in Figure 5. This shows the pinning profile for several different values of the ratio of strong pinning to weak pinning strengths (D). This parameter is a measure of pinning strength. Large values for the pinning strength parameter correspond to strong pinning where $R_c = a_o$. Smaller values show increasing regions of weak pinning behavior ($R_c > a_o$) until at $D = 10^{-3}$ the profiles show weak pinning behavior over the entire range of reduced field. In this figure (Figure 5) the transition from weak pinning to strong pinning is smoothed by assuming a Gaussian distribution of pinning strengths. The effect of different distributions is shown in Figure 6. Here the parameter D was determined by forcing the peak in F_p to fall at the same reduced field for each distribution. The resulting pinning profile is shown for point, Gaussian, Poisson and square root distributions.

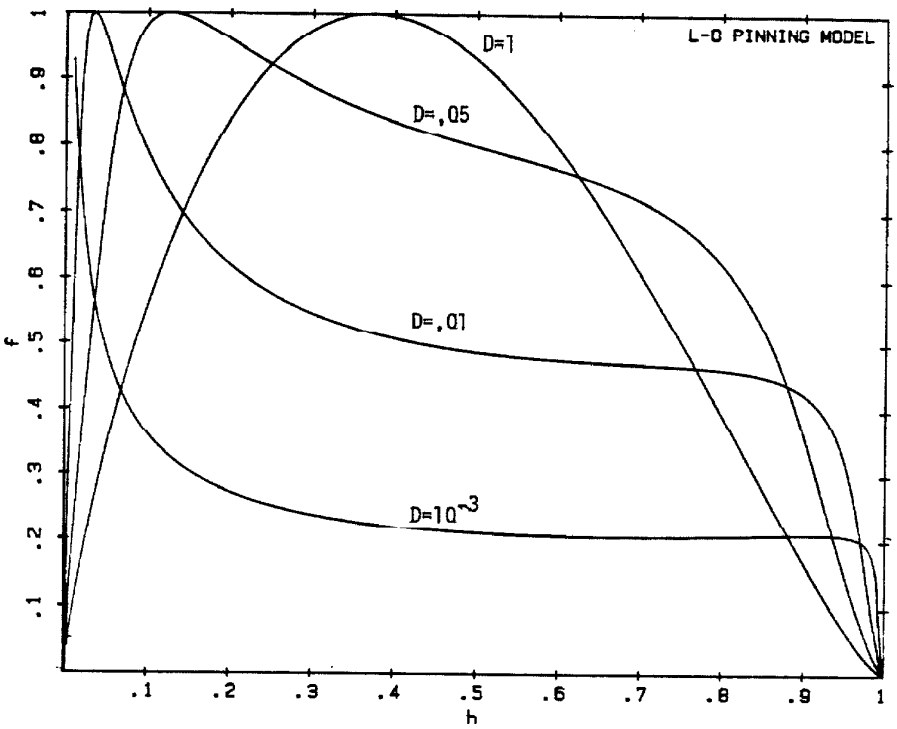

Figure 5. Pinning profiles generated by Larkin-Oychinnikov pinning model for different values of the pinning strength parameter D.

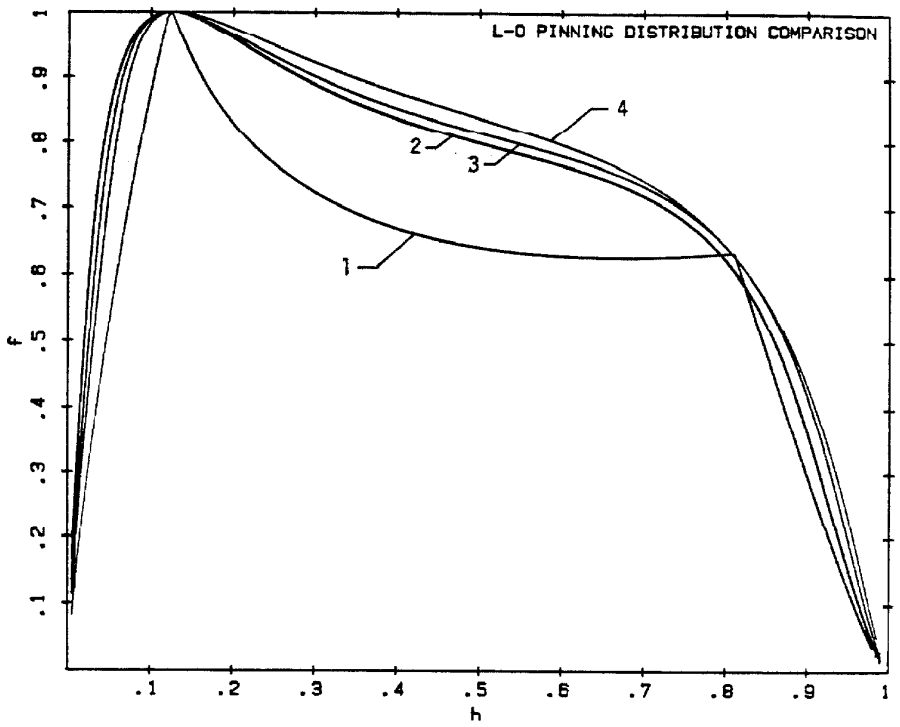

Figure 6. Pinning profiles generated by Larkin-Ovchinnikov pinning model. Numbers on graph refer to distributions of pin strength (k) in the following manner:

1. Point $\rho(k) = \delta(\langle k \rangle)$

2. Gaussian $\rho(k) = \frac{2}{\pi\langle k \rangle} e^{-\frac{1}{\pi}(k/\langle k \rangle)^2}$

3. Poisson $\rho(k) = \frac{1}{\langle k \rangle} e^{-(k/\langle k \rangle)}$

4. Square Root $\rho(k) = \frac{1}{2\langle k \rangle} e^{-(k/\langle k \rangle)^{1/2}}$

B. Amorphous Metals

1. Formation and Structure

The amorphous materials in this study were formed by three preparation techniques the mechanics of which will be described in the experimental section of the thesis. The techniques were: 1) rapidly quenching from the melt, 2) sputter deposition, and 3) ion beam mixing. Strictly speaking, the first process is the only one of the three which produces a glass, a glass being by definition an amorphous material formed from a liquid phase. However each of the processes do produce metastable amorphous phases by quenching out atomic motion which would result in a rearrangement of the structure to a more stable (crystalline) phase.

In producing an amorphous material by rapidly quenching from the melt it is necessary to start with a system where the liquid structure is as stable as possible relative to the crystalline structure. Thus, amorphous materials formed by this technique occur in alloy systems which exhibit a deep eutectic. In these systems the free energy of the liquid is decreased relative to that of the crystalline phase by one of three possible mechanisms, a large negative heat of mixing in the liquid state, a positive heat of mixing in the solid state or the existence of a competition between two crystalline structures of different symmetry which can act to frustrate the formation of either crystalline phase. The result of a stabilized liquid phase is that the range in temperature between where the crystalline phase

becomes more stable than the liquid phase (i.e., the melting point T_m) and the temperature where the atomic mobility decreases to a point where crystallization cannot occur (i.e., the glass transition temperature T_g) is small. Crystallization occurs by a nucleation and growth process.[36] The total free energy of a small region of crystalline material embedded in a liquid which has been cooled below its melting temperature contains a contribution due to the positive crystal-metal interface energy, which results from the surface atoms being frustrated in their attempts to occupy the equilibrium position which respect to both the liquid and solid phases, and the negative volume term representing the fact that the crystalline phase is the equilibrium phase at temperatures below T_m. Thus crystalline nuclei must be larger than a critical size (characterized by a radius r_c) in order that their energy will decrease by growing. A collective motion of several atoms is required to form a stable nucleus. If the temperature range between T_m and T_g is sufficiently small, then a rapid quench is often sufficient to freeze out atomic motion before nucleation and growth of the crystalline phase can occur.

The metallic systems which can be quenched into an amorphous phase in this manner can be grouped into three classifications. One group of glass forming systems is systems which consist of one or more transition metals (e.g., Fe, Pd, MoRu,Ni) and one or more metaloids (e.g., Si, P, B, SiB). Amorphous phases formed in these systems usually consist of about 80% transition metal and 20% metaloid.

A second class of glass forming systems consists of an early transition metal and late transition metal near their eutectic composition. Examples are ZrCu, NbNi and YFe. A third class of glass formers consists of a transition metal in combination with a lanthanide or actinide. Examples are GdFe and GdCo.

In a sputtering process the atoms are expelled from a source and hit the substrate in a random position. What happens to atoms which hit the substrate is a function of their energy upon hitting the substrate and the substrate temperature. If the initial energy is low and the substrate temperature is below T_g, the collective motion required to form a crystalline phase will not occur and an amorphous phase will be formed. The ease of amorphous phase formation is still subject to the same considerations as in liquid quenching. If the system can form a simple single phase crystalline structure the atomic motions required for crystallization are not extensive or complex and the system will crystallize with relative ease. However, if the equilibrium structure consists either of two phases or a complex crystalline structure substantial atomic motion is required for crystallization. Thus sputtering will tend to achieve an amorphous phase in the same types of systems as liquid quenching. However, by controlling the deposition parameters, including substrate temperature, amorphous phases can be formed in systems for which an amorphous phase is not readily obtained by rapidly quenching from the melt.

The third method of amorphous phase formation is by ion beam mixing. Here an equilibrium structure is randomized and de-

stabilized by bombardment by energetic (300 keV) inert gas ions. The original structure consists of layers of at least two different types of crystalline elements. As the ions hit they cause a cascade event which mixes the layers and randomizes atomic positions. If the resulting composition is one that, for the reasons given above, favors amorphous phase formation, then crystallization will be suppressed.

The structural information on amorphous materials is obtained by various diffraction experiments (x-ray, neutron, electron). The intensity as a function of scattering angle displays no sharp bragg diffraction peaks but has broad smooth bands. From a Fourier transform one can obtain a radial distribution function $G(\rho)$. This is the average probability that a given atom will have a neighbor at a distance ρ away. The radial distribution function for sputtered MoRuB and splat cooled MoRuB are shown in Figure 7.[37]

C. Transformation from the Amorphous State

At elevated temperatures a metallic glass will eventually transform to the equilibrium crystalline structure. Often this occurs via a two or more step process involving a metastable crystalline phase. The various possible crystallization reactions in amorphous alloys have been analyzed in terms of a hypothetical free energy versus concentration diagram by Köster and Herold.[38] Of the three types of crystallization reactions (polymorphous, primary and eutectic) two involve composition segregation. Primary crystallization of one of

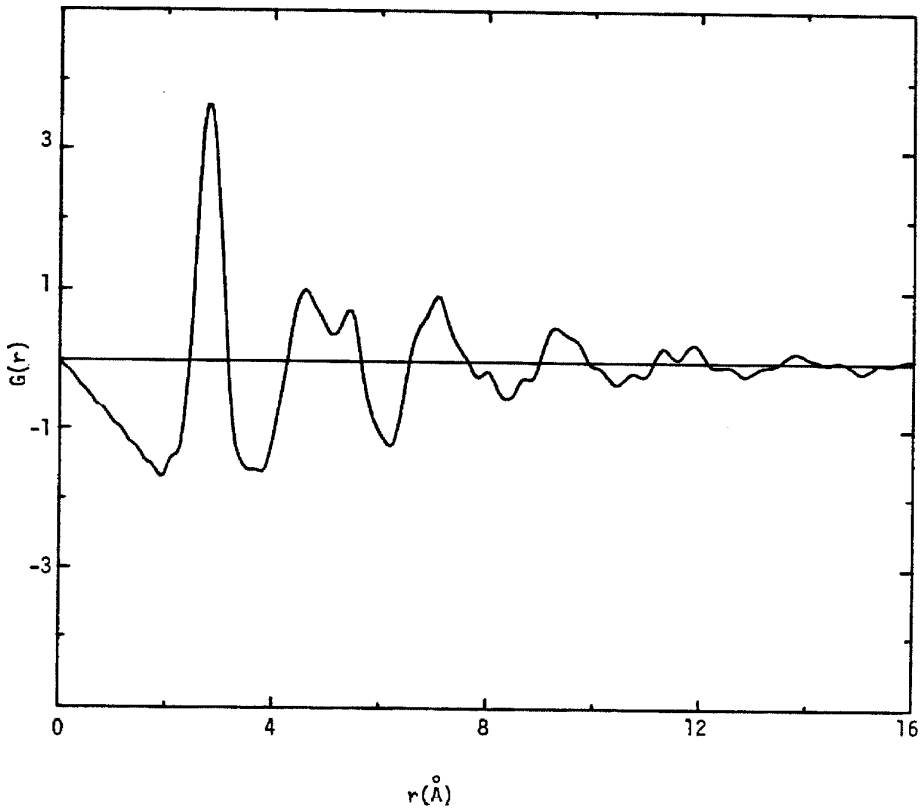

Figure 7. Radial distribution function for sputtered $(Mo_{0.6}Ru_{0.4})_{82}B_{18}$.[37]

the terminal phases enriches the remainder of the amorphous phase in the component for which the crystallizing phase is deficient. Eutectic crystallization (crystallization into a two-phase morphology) can often occur at the glass composition but the components must separate into two chemically distinct phases which involve a compositional segregation.

The question arises as to whether metallic glasses can phase separate into two amorphous phases of different composition and possibly structure before crystallization. If a glass forms due to competition between two crystalline phases, then it might be that they also form two amorphous phases each resembling one of the crystalline phases in composition and chemical short range structure. Evidence for the existence of two types of short range order has come from Mosbauer measurements,[39] evidence for two amorphous phases has come from TEM,[40] specific heat,[41], and atom probe field ion microscope.[42] Further evidence for phase separation from superconductivity measurements will be presented in this study.

Spinodal decomposition[43] is one possible mechanism for separation into two amorphous phases of differing composition. Cahn[43] has shown that a system is unstable with respect to fluctuations in composition if $\frac{\partial^2 f(c)}{\partial c^2} < 0$ where f is the Helmholtz free energy per unit volume of a homogeneous material of composition c. The condition $\frac{\partial^2 f}{\partial c^2} = 0$ defines the spinodal region of the phase diagram, inside of which one finds the system unstable with respect to composition segrega-

tion. The strain energy associated with a composition gradient will help stabilize the homogeneous solution resulting in a more restrictive condition for unstability $\frac{\partial^2 f}{\partial c^2} < -\frac{2\eta E}{1-\nu}$ where η is the linear expansion per composition change ν is Polsson's ratio and E is Young's modulus. The shortest wave length compositional segregation for which the system is unstable is denoted as B_c and given by $B_c = \frac{-1}{2K}\left[\frac{\partial^2 f}{\partial c^2} + \frac{2\eta^2 E}{1-\nu}\right]^{1/2}$ where K is the linear coefficient relating free energy to a compositional gradient. By examining the kinetics of spinodal decomposition Cahn has shown that compositional segregations of wavelength $B = 2B_c$ will preferentially grown in the early stage of decomposition of a homogeneous material.

II. Experimental Procedures

A. Sample Preparation

1) Rapid Quenching from the Melt

Ingots of the desired composition were formed by melting the proper constituents on a water cooled silver boat in a gettered argon atmosphere. The 2 to 5 gm ingots were turned over and melted several times, then broken, checked for obvious segregation and then re-melted in an attempt to insure homogeneity. The ingots were weighed after melting to insure that no appreciable amount of any constituent was lost. The compositions reported are the nominal composition of the ingot.

Two melt quenching techniques were used in this study. The first is the piston and anvil [44] method shown schematically in Figure 8. The ingots are first broken into pieces and about 30 to 50 mg of sample is placed in a quartz tube which is then placed inside a cylindrical graphite succeptor. The graphite succeptor is then heated by an R-F generator and the sample is melted. The molten droplet is then ejected with a helium jet downward from the end of the tube. As the droplet falls it intercepts a beam of light which triggers a pneumatically driven piston. The droplet is caught between the piston head and an anvil which are both made of a CuBe alloy heat treated to maximize hardness and thermal conductivity. The anvil is cushioned by a helium filled chamber to prevent bounce. The droplet is "spatted" into a foil which rapidly solidifies at rates

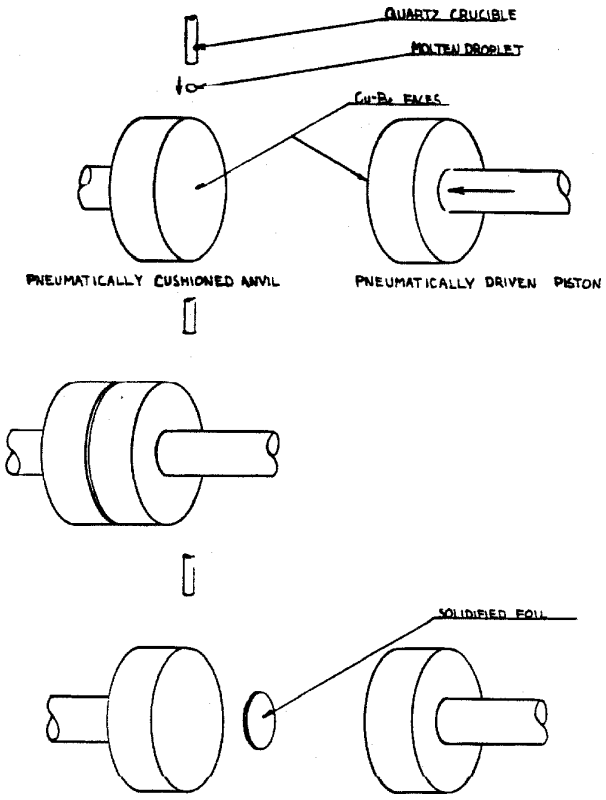

Figure 8, Piston and anvil splat quenching technique.

estimated to be about 10^6 K/sec. The resulting foil is about 1 cm in diameter and 25 - 50 μm thick.

The cooling rate achieved by this method is a function of many parameters. The thermal conductivity of the piston and anvil material, the piston speed, the amount of bounce the piston experiences upon hitting the anvil and the alignment of the piston and anvil are all possible sources for variation in cooling rates. It is not surprising that many samples which are quenched with this apparatus are not totally amorphous but have a varying amount of crystalline inclusions formed during the quenching process. The crystalline phase often has a small crystal size (50 - 100 Å) and the crystals are uniformly dispersed in the sample. In some cases the crystalline phase is a non-equilibrium structure. Thus the study of a variation in cooling rates is an interesting prospect. Unfortunately, the cooling rate is very hard to control in the piston and anvil apparatus.

The second method for rapid quenching from the melt is the melt spinning technique. This technique was developed in the 1950's by R. B. Pond at Battelle [45], and was a fairly well developed technology at the time of the instigation of this study. However, there was no melt spinning apparatus in our laboratory until the construction of one by the author as part of this study. In this technique 2 to 3 gm of sample is placed in a quartz crucible which has a 0.1 to 2.0 mm hole in the bottom. The crucible is then placed in an induction coil and the top is connected to a hose which runs to a sealable

ballast of about 1 liter volume. The bottom of the crucible is located above the upper surface of a copper wheel about 1 cm wide and 10 cm in diameter, which is connected to a variable speed D.C. motor. The entire assembly motor, wheel, crucible and coil is inside a vacuum chamber which has coaxial electrical feedthroughs for the R. F. power. The chamber is then pumped out using a mechanical pump and backfilled with inert gas to the desired pressure (usually several torr). The ballast is also pumped out and a valve is shut between the ballast and the crucible. The ballast is then filled to a pressure greater than the vacuum chamber. The motor is then turned on to the desired speed ($\sim$ 10,000 RPM). The sample is melted by the R. F. induction and the valve is opened between the ballast and the crucible. This causes the molten sample to squirt down onto the rapidly spinning wheel where it solidifies and comes off as a ribbon of rapidly quenched material. By variation of the wheel speed, crucible orifice diameter and ballast pressure, the cooling rate can be controlled. The maximum cooling rate obtained by this method is estimated to be about 10^6 K/sec.

The width of the ribbons made by this technique can be controlled somewhat by varying the orifice diameter and ballast pressure. However, instabilities in a flat sheet jet of molten metal develop within a millimeter or so after leaving the nozzle. A melt puddle can be stabilized by the bottom of the crucible as shown in Figure 9 allowing a wide ribbon to be extracted from the bottom of the melt by the wheel. This method has allowed formation of ribbons as wide as

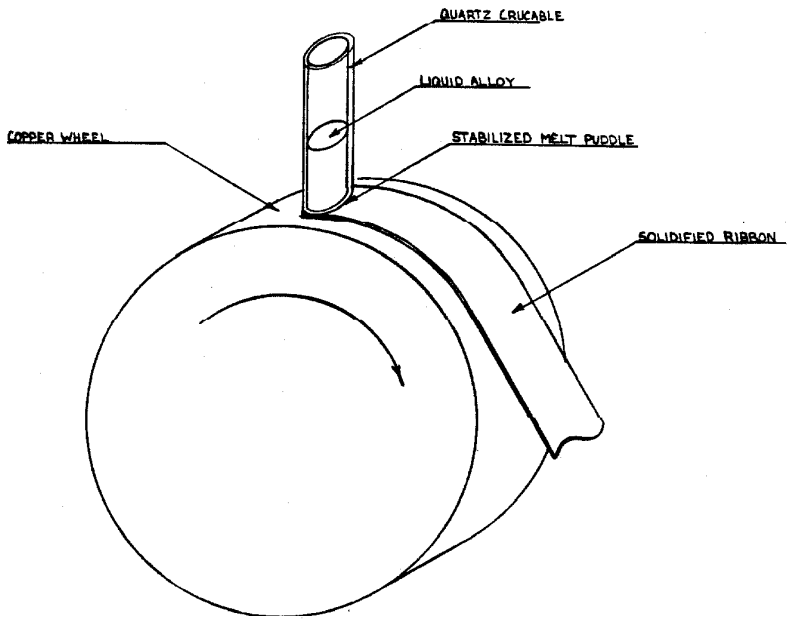

Figure 9. Melt spinning apparatus.

15 cm [46]. High melting point alloys tend to freeze to the nozzle when this method is employed. An induction coil which has a double winding near the crucible orifice was constructed to help with the problem but this remains a problem and is often a limiting factor in the fabrication of wide ribbons of high melting point materials.

2) Sputtering

Sputtered samples of composition $(Mo_{0.6}Ru_{0.4})_{82}B_{18}$ used in this study were prepared by M. Mehra and Anil Thakmr at the D.C. Magnetron (S-gun type) facility at J.P.L. Targets of the desired composition were prepared by mixing of fine mesh (<600) powders of the appropriate constituents, compressing and heating to form the desired ring shape target. A potential of ∿400 V D.C. was produced at the cathode target to produce a glow discharge in the argon atmosphere. This produced Ar^+ ions which were accelerated to the target and produced sputtering of neutral atoms. The substrate was held at ground relative to the cathode. A magnetic field produced a force at right angles to the velocity of the electrons in the glow discharge which resulted in a spiral path. This served two functions; first, it prevented the electrons from striking the substrate which would produce unwanted substrate heating and second, the energetic electrons circling in the glow discharge region ionized argon atoms increasing the sputtering rate, allowing substantial sputtering rates at relatively low Ar pressures (∿5 μ). The samples

produced in this system were 2 - 5 μm thick. The substrates used were Pyrex slides. The effect of a variation in Ar pressure was investigated.

3) Ion Beam Mixing

Two elemental metals were deposited by e^- beam evaporation in alternate layers each about 50 Å thick to produce a film about 500 Å thick. The thickness of the layers was controlled to produce the desired composition. The substrate used was a Si wafer with the surface oxidized to produce an inert Si O_2 layer. The films were then placed in a 300 keV $Xenon^+$ ion beam. The total irradiation dose ranged from $1x10^{15}$ to $2x10^{16}$ Xe/cm^2. Rutherford back scattering showed no structure in the film after irradiation indicating a destruction of the layered structure. The x-ray diffraction (Reed camera) on the ion mixed films revealed an amorphous structure. The xenon ions were distributed through the thickness of the film with a Gaussian distribution with a width equal to about the film thickness.

B. Superconducting Measurements

1. Superconducting Transition Temperature

The superconducting transition temperature was measured by two techniques, each taking advantage of one of the manifestations of the superconducting state. An A.C. inductance bridge was used to measure the inductance of the sample to determine the temperature at which a small ($\sim$1 gauss) A. C. (1000 Hz) field was expelled from the superconductor (Meissnor effect). About 10 mg of sample is placed in the center of one of three measuring coils on the probe which are embedded in a copper probe. The probe end is then sealed in a brass can which is evacuated and backfilled to 10 cm He^4 gas pressure. A Ge resistance thermometer is in intimate contact with the sample area. The entire assembly is then placed in liquid He^4. A small external signal is then applied to the A. C. bridge which has a reference coil on one arm and the sample coil on another. The bridge is balanced by a variable inductor and the signal passes through a lock-in amplifier. As the temperature is increased by a resistance heater, the sample is driven normal. The field penetrates the sample which changes the inductance of the sample coil producing an imbalance in the A. C. bridge. This signal is detected and amplified by the lock-in and then fed to the y-axis of an x-y recorder, the x-axis of which is monitoring temperature. By pumping on the He^4 bath, temperature as low as 1.2 K can be accessed.

Transition temperatures were also measured resistively by the standard four point probe technique. The probe used is one constructed

by the author for the purpose of measuring critical currents. Details of the electrical contacts will be presented later in this section. The probe can be operated in two modes, with the sample holder and sample immersed directly in liquid He^4 or with the sample holding assembly sealed in a can with a partial pressure of He^4 gas. When the probe is operated in the immersed mode, the vapor pressure of He^4 is used to measure temperature. The vapor pressure of the bath is controlled by a Lake Shore constant pressure vacuum valve. Two samples can be measured simultaneously in this mode. When the probe is sealed in the can, a carbon resistance thermometer is used to measure temperature and a resistance heater used to vary the temperature. A 10 μA current is run through the thermometer and can also be used as a sample current. Unfortunately, there was a typical temperature difference between the sample and thermometer of 0.1 K. This was due to the lack of intimate contact between the sample and thermometer block and the heavy current wires running to the sample. These problems are inherent in a probe designed for high current capability and operation in a submersion mode.

2. Upper Critical Fields ($H_{c_2}(T)$)

Upper critical fields are also measured by the four point probe method. Both modes of probe operation can be used and the temperature control is the same as in T_c measurements. The field is produced by a superconducting solenoid made of NbTi copper clad wire. The specifications for the magnet are given in Table 2. The field as a

RATED CENTRAL FIELD.	60 kilogauss @ 4.2 K
RATED CURRENT.	69.2 amperes
MAXIMUM TEST FIELD	69 kilogauss @ 4.2 K
FIELD TO CURRENT RATIO	867.3 Gauss/ampere
HOMOGENEITY.	±0.5% over 1 cm^3 at center
INDUCTANCE	∿1.7 Henries
CHARGING VOLTAGE	1.5 volts
CLEAR BORE	1.5 inches
OVERALL LENGTH	4.8 inches
MAXIMUM OUTSIDE DIAMETER	4 inches
RESISTANCE	213 ohms at room temperature

TABLE 2. Specifications for superconducting Nb-Ti solenoid magnet.

function of position away from the longitudinal center of the solenoid can be calculated and easily measured using a sample with a known critical field. The results are summarized in Figure 10. The current leads each consist of 10 braided tubes each containing 19 22-gauge tinned copper wires. This is to maximize the cooling surface to cross section area ratio of the current leads.[47] The magnet is rated at 60 kG at 4.2 K but can routinely go to fields as high as 65 kG. While pumping on the bath the maximum field obtained was 80 kG. A 10 Ω shunt resistor is in parallel with the magnet to prevent damage during a quench. The magnetic field is measured by running the magnet current through a 0.01 Ω precision resistor and converting the voltage produced to field in k Gauss with a special purpose digital volt meter. The output of the precision resistor can also be fed into a chart recorder. The voltage across the sample is measured by a Kiethley microvoltmeter which has a 0-10 V analogue output which can be fed into a chart recorder. In this manner resistance versus field can be obtained at several temperatures. The transition midpoint is taken to be H_{c2} and the width of the transition is the difference between the 10% and 90% transition points.

Upper critical fields were also measured at the Francis Bitter National Magnet Laboratory at Massachusetts Institute of Technology. Magnetic fields up to 220 kG are generated by water cooled Bitter type normal conducting magnets. The probe at this facility also has two

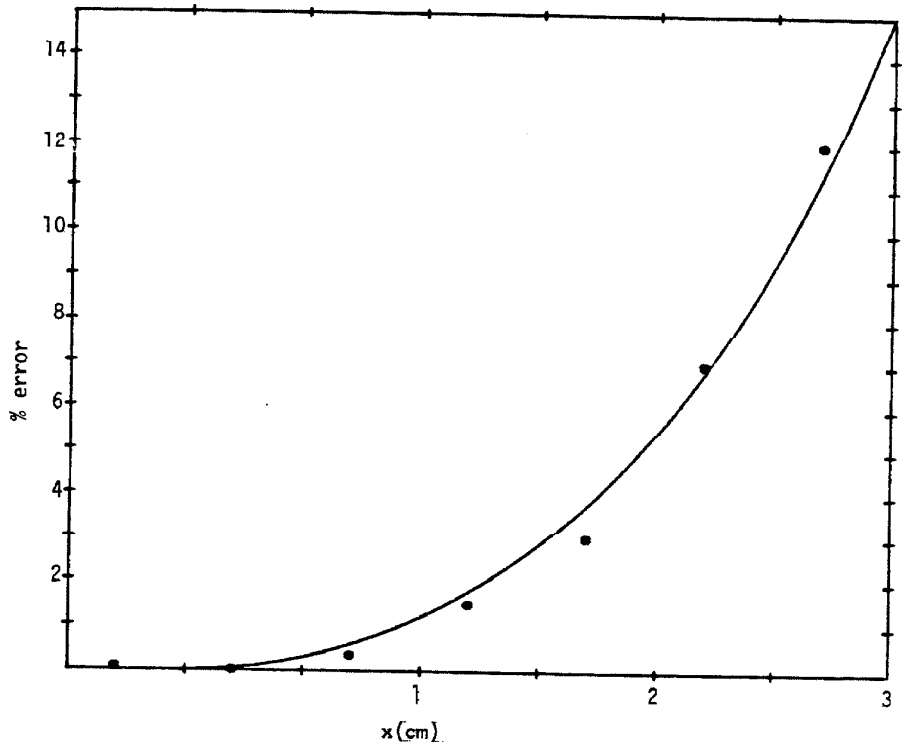

Figure 10. Reduction in field as a function of position (x) along the axis of the solenoid measured from the center position. Solid line is theoretically expected reduction.

modes of operation very similar to the Caltech probe. However, when operating in the sealed mode the temperature is controlled by a Lake Shore temperature controller and measured by a capacitance thermometer which is not affected by the magnetic field.

3. Critical Current Measurements

The probe used for critical current measurements has been described in the resistive T_c and $H_{c_2}(t)$ sections. Due to the large critical currents carried by some of the materials in this study, the probe was designed to carry 100 amps to the sample. The current leads were 10 ga copper wire leading down to superconducting multifillamentary NbTi BCC copper clad wire which carried the current the last 10 cm to the sample. The current contacts to the sample were made by one of three ways. For high current density materials it is very important to have low resistance ($\lesssim 1\ \mu\Omega$) current contacts. One way to achieve this is to spot weld gold pads to the ends of the sample and then solder the gold to the current tabs on the probe. This sometimes resulted in sample breakage during the spot welding process. A second method used to achieve low resistance contacts was to electroplate copper on the ends of the sample and solder the electroplated sample to the current tabs on the probe. A low pH cyanide type plating bath provides very good adhesion. In both these methods the voltage leads must be attached separately in the form of spot welded latenum wires. The third type of current contact is easy to use and is adequate for low

critical current density materials and for films on substrates. This contact is made by pressing the sample into an indium pad. A glass plate across the back of the sample is pressed onto the sample as shown in Figure 11. Berylum-copper alloy springs push against the sample for voltage contacts in this sample mounting method allowing for very quick sample mounting. Also no sample heating occurs, spot welding, meaning a minimum amount of possible sample damage.

The voltage along the sample was measured with a Kiethley microvoltemeter. In principal, the critical current is defined as the maximum current for which the voltage along the sample remains zero. However, due to instrument sensitivity and noise problems, this point is not measurable. Two different types of operational definitions exist for critical current. The first is a threshold of an easily measurable voltage. Critical current at a fixed field and temperature is defined where the voltage level (often 1 μv is used). This definition has some disadvantages. The difference between the true critical current and the measured value is dependent on field since as mentioned in this theory section of the thesis the slope of the I-V curve is proportional to H/H_{c_2}. Also, sudden flux jumps and thermal noises make it difficult to accurately determine exactly at what current the threshold is crossed. The second type of operational definition involves some type of extrapolation procedure. The I-V curve is measured and extrapolated to zero voltage. This works well and is easy if there exists a well defined linear region in the I-V curve. However, in amorphous materials the I-V curves (Figure 12) show a considerable amount of

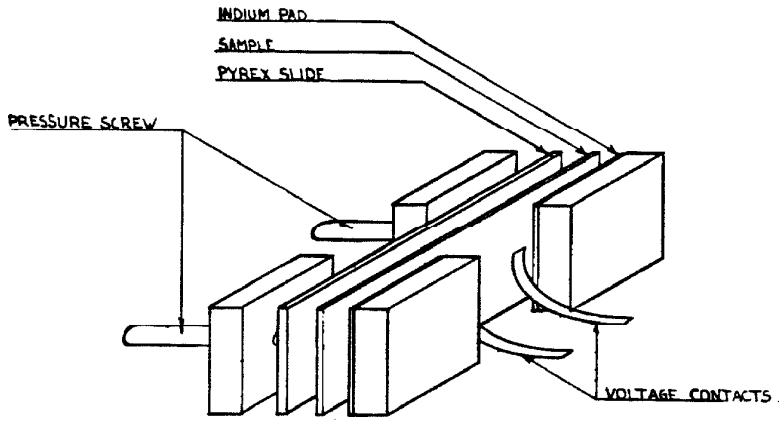

Figure 11. Critical current probe end showing voltage and current contacts.

curvature and the exact current for which the voltage becomes non-zero is difficult to obtain by linear extrapolation.

In the present study both types of critical current criteria were used. In the first method, the current source was switched by a relay driven by a function generator at about 1 Hz. This was to eliminate training effects. The current was gradually increased until a 2 μV difference between the sample voltage for each current direction was observed. The second method involved computer control of the experiment using a MINC 11/23. The current is controlled with the D/A module of the MINC. The sample voltage is read by feeding the analogue output of the Kiethley into a HP voltmeter which was a digital output. The signal is then fed into the digital input module on the MINC. The controlling program works in the following way: The current is increased until the sample voltage exceeds a predetermined value ($\cong$ 1 μV). Then the current continues to increase and values for I and V are stored in an array. A linear fit is performed. The current values for a voltage window between 0 and 10 μv are determined by this fit. The sample voltage is then measured at 20 evenly spaced points between these current values. At each point the current is set, the sample voltage measured, the current is reversed, and the sample voltage is measured again. The average value of the sample voltages is stored. The data are then fit to a second order polynomial. Typical data and fit are shown in Figure 12. The noise in the voltage data often prevents an extrapolation

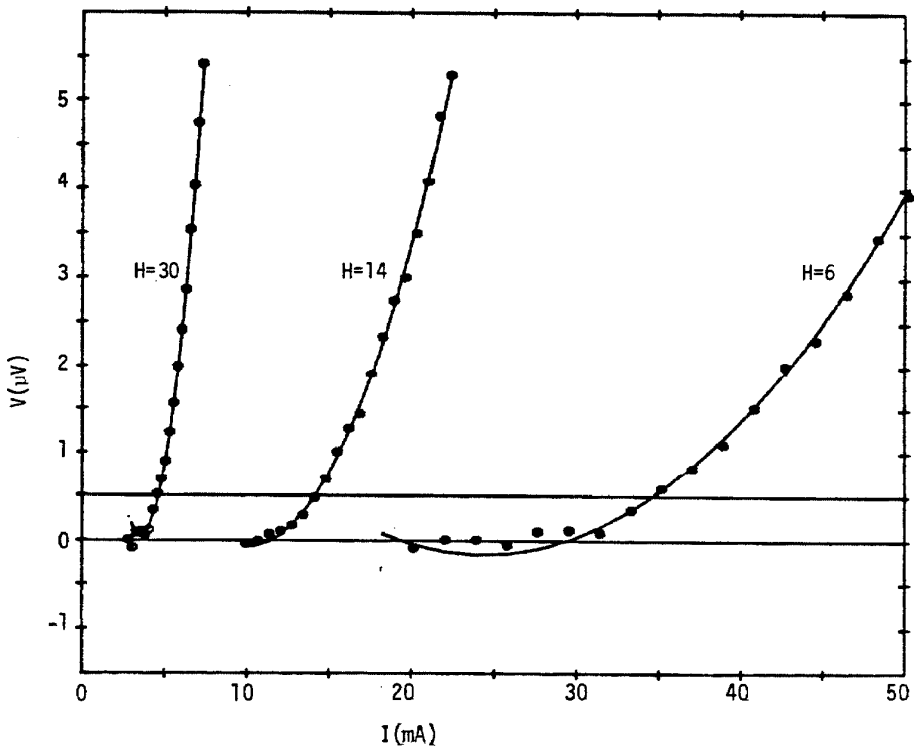

Figure 12. Typical I-V curves at different applied fields taken during a computerized critical current run. Points are data values and solid curves are second order polynomial fits. Also shown is a solid line at V = 0.5 μV, corresponding to a 1/2 μV criteria.

to zero voltage, but an extrapolation can be performed to voltages as low as 0.5 μV. A comparison of flux pinning profiles obtained by using 0.5, 1, 2 μV criteria showed no appreciable difference in shape of the flux pinning profile. Furthermore, changes in amplitude of the flux pinning force are also independent of criteria as long as comparisons are made between measurements made using the same criteria.

IV. Measurements on Metallic Glasses

A. Flux Pinning

1. Pinning by Crystalline Precipitates

The effect of a varying amount of crystalline phase inclusions in an amorphous matrix was investigated. The motivation for this study came from both theoretixal and practical applications. The low critical current values typical of purely amorphous materials makes them an ideal matrix to study the pinning by a known type of inhomogeneity. In addition the high H_{c_2} values found in amorphous materials, their desirable mechanical properties, and their insensitivity to degradation in superconducting properties by neutron irradiation suggest that amorphous materials may be suited to applications involving the generation of large magnetic fields in high neutron flux environments such as in magnetic containment of a fusion plasma. However, the generation of large magnetic fields requires high currents and thus an increase in the critical current density in amorphous materials is required before they are useful in such applications. The introduction of small amounts (2-5%) crystalline inclusions is shown to increase dramatically the critical current in comparison to purely amorphous material.

The samples used in this study were of composition $(Mo_{0.6}Ru_{0.4})_{80}Si_{10}B_{10}$. They were prepared by the piston and anvil method described in the experimental section of this thesis. As pointed out in that section, a large variation in the cooling from sample to sample is characteristic of this method of sample preparation.

Foils which contained varying amounts of crystalline inclusions were produced. The x-ray scan of a sample which contains very few crystalline precipitates is shown in Fig. 13(a). The very slight irregularities in the broad amorphous band indicates the presence of a small amount of crystalline phase. The volume fraction of such material can be roughly determined by estimating the ratio of the integrated area under these peaks and comparing it to the area of the broad band on which they are superimposed. Using this procedure gives an estimate of .1-.4% crystalline material. Fig. 13(b) shows an electron micrograph of a region of the sample containing two spherical crystalline inclusions. Several regions of the sample were viewed and the probability of finding a crystalline inclusion in a typical field of view such as the one shown was judged to be about 1/2. All crystals observed were spherically shaped and had sizes typical of those inclusions shown. From this information the volume fraction of crystalline phase was estimated to be about .1-.4% in agreement with estimates based on x-ray diffraction. Fig. 13(c) shows an electron diffraction pattern of a typical region of the sample. Note the series of diffuse bands characteristic of an amorphous matrix.

Figure 14 contains corresponding data for a sample which contains substantially more crystalline phase. Analysis of the x-ray diffraction peaks (Fig. 14) allows the identification of a single crystalline phase having the $D8_b$ (σ-phase) structure found in the equilibrium Mo-Ru system.[48] By the method described above, the volume fraction of

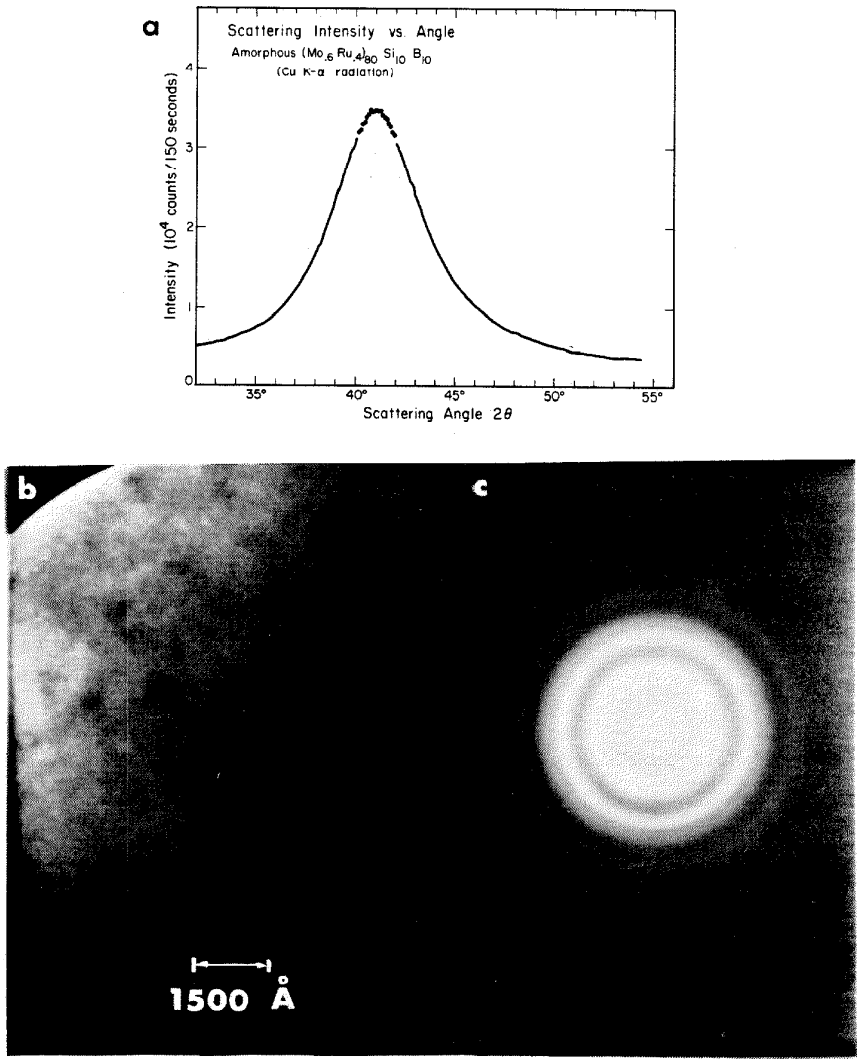

Figure 13. Results of structural analysis of amorphous $(Mo_{0.6}Ru_{0.4})_{80}Si_{10}B_{10}$ with 0.1-0.4% crystalline inclusions. Shown are a) x-ray diffraction pattern, b) electron micrograph, c) electron diffraction pattern of a typical area.

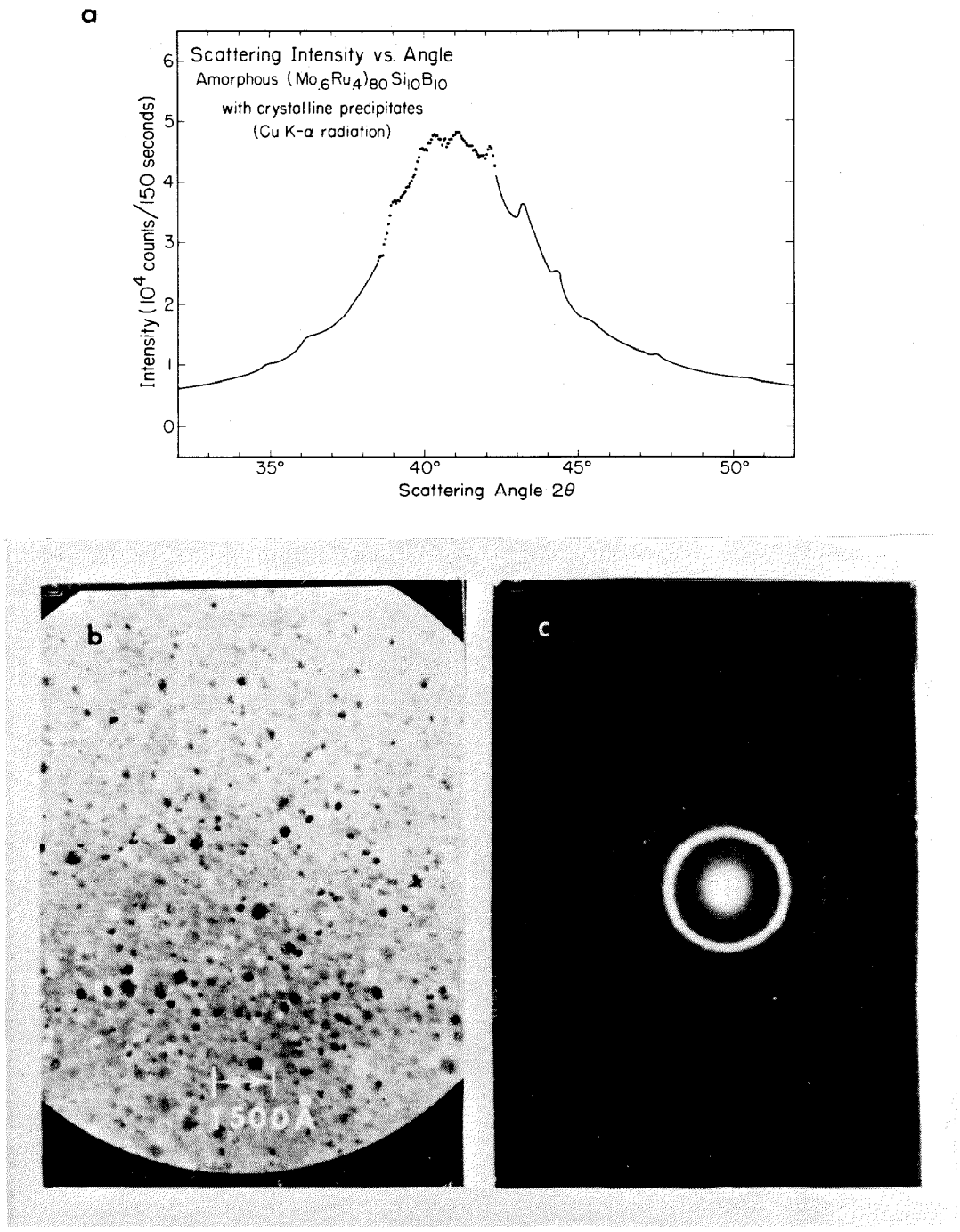

Figure 14. Results of structural analysis of amorphous $(Mo_{0.6}Ru_{0.4})_{80}Si_{10}B_{10}$ with 2-4% crystalline inclusions. Shown are a) x-ray diffraction pattern, b) electron micrograph, c) electron diffraction pattern.

crystalline phase can be estimated from the x-ray diffraction pattern to be about 3-5%. The electron micrograph shown in Fig. 14(b) shows that the precipitate particles are spherical with a characteristic dimension of 100-200 Å, much smaller than those shown in Fig. 13(b). From this morphology, one infers first, that the nucleation rate of these particles under the liquid quench conditions of the sample was high. Second, the growth of the particles was limited by their high density. The volume fraction of crystalline phase can be roughly estimated from Fig. 14(b) to be about 2-4% which is in reasonable agreement with estimates based on x-ray diffraction. The density of particles in the sample was also estimated from Fig. 14(b) to be about 10^{15} particles/cm^3 or about 10^3 times higher than the sample described in Fig. 14. The electron diffraction pattern shown in Fig. 14(c) is characteristic of an amorphous matrix with a high density of small crystalline precipitates. We use the term small to indicate that many particles are located within the dimensions of the beam aperture used in diffraction.

Superconducting transition temperatures were measured directly utilizing an ac induction bridge. The resistive T_c was determined from the H_{c_2} measurements. The T_c determined by these two methods was consistent to within 0.1 K. Table 3 shows the transition temperatures for the two samples discussed here. Note that one effect of crystalline inclusions is to raise significantly T_c. The σ-phase of MoRu has a reported T_c of 7 K.[49] If the inclusions are larger than a few

Structure	$T_c(k)$	$\left.\frac{dH_{c_2}}{dt}\right\|_{T_c}$ $(\frac{kOe}{D})$
Amorphous	5.1±0.1	27.0±2
Amorphous plus crystalline inclusions	6.5±0.1	23.5±2

TABLE 3. Structure, superconducting transition temperature, and critical field gradient for $(Mo_{0.6}Ru_{0.4})_{80}Si_{10}B_{10}$ samples studied.

coherence lengths they will become superconducting at a higher temperature than the surrounding matrix (T_c = 5.1 K) and raise the apparent T_c of the entire sample through the proximity effect. [50,51] Using Ginsburg-Landau Theory we can determine the value of the coherence length for the amorphous $(Mo_{.6}Ru_{.4})_{80}Si_{.6}B_{10}$ matrix. It should be noted that the coherence length of the σ-phase is likely to be somewhat different from that of the amorphous matrix. The diameter of the inclusions is 2-5 times the calculated coherence length of the amorphous matrix. The increase in T_c observed for the two-phase sample can be compared to that predicted by the proximity effect calculations of Silvert and Singh. [51] Their calculation involved isolated superconducting spheres of given T_c imbedded in a matrix of lower T_c. In the present case, the crystalline inclusions are typically separated by only several coherence lengths. Therefore the solution to the proximity effect problem should include a linear combination of local solutions which are strongly overlapping. As a result, a somewhat higher T_c should be observed for the sample as a whole than predicted by Silvert and Singh for isolated particles. This seems to be consistent with our data which gives a resistively measured T_c close to that of σ-phase Mo-Ru.

The results of upper critical field (H_{c_2}) measurements are shown in Fig. 15. Also shown are linear extrapolations of the data, and curves calculated from the Maki theory [22] ignoring the paramagnetic limiting and spin orbit effects. Note that the linear region of the data is more extensive than is predicted by the theory. This

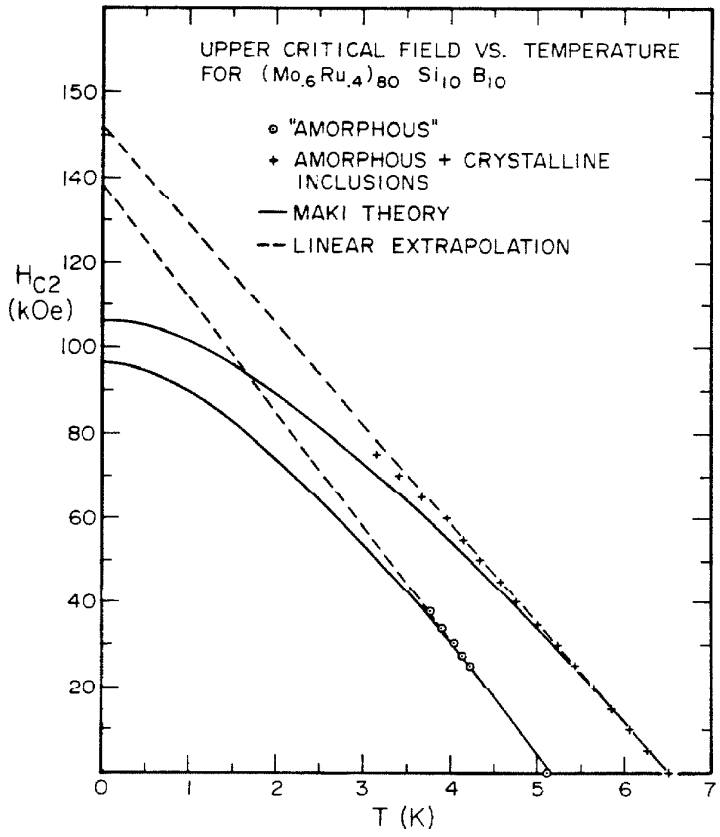

Figure 15. Upper critical field H_{c_2} versus temperature for amorphous and amorphous plus crystalline inclusions $(Mo_{0.6}Ru_{0.4})_{80}$ $Si_{10}B_{10}$. Also shown are linear extrapolations to the data and curves from the Maki theory fit to the data.

behavior has been previously observed to be typical of amorphous superconductors.[52,53] The critical field gradient $\left.\frac{dH_{c_2}}{dT}\right|_{T_c}$ (Table 3) is somewhat lowered by the presence of a crystalline phase. This is to be expected due to the longer mean free path and lower resistivity characteristic of crystalline materials.

Critical current measurements performed on the two types of samples studied showed very significant differences. Fig. 16(a) shows the critical current as a function of magnetic field strength for the sample with a very small (.2-.4%) amount of crystalline phase (the sample described by Fig. 14 henceforth referred to as the amorphous sample). Compare this to Fig. 16(b) which is the corresponding data for the sample with 2-5% crystalline phase described by Fig. 15 (henceforth referred to as amorphous plus crystalline). The critical current is two to three orders of magnitude higher at a given field strength. For example, at 4.2 K and 20 kOe the sample without crystalline inclusions has J_c of 6 amps/cm^2, while the sample with crystalline inclusions has J_c of about 6×10^3 amps/cm^2. This difference can be attributed to the flux pinning action of the crystalline inclusions. The pinning forces are most likely to arise from difference in superconducting parameters of the two phases involved.

To compare the experimental results with the flux pinning theories it is helpful to construct a pinning profile $F_p(h)/F_{pm}$. Fig. 17 shows the pinning profile for the amorphous sample. The main features of this profile are the peak at low h ($\sim$0.15) and the near linear

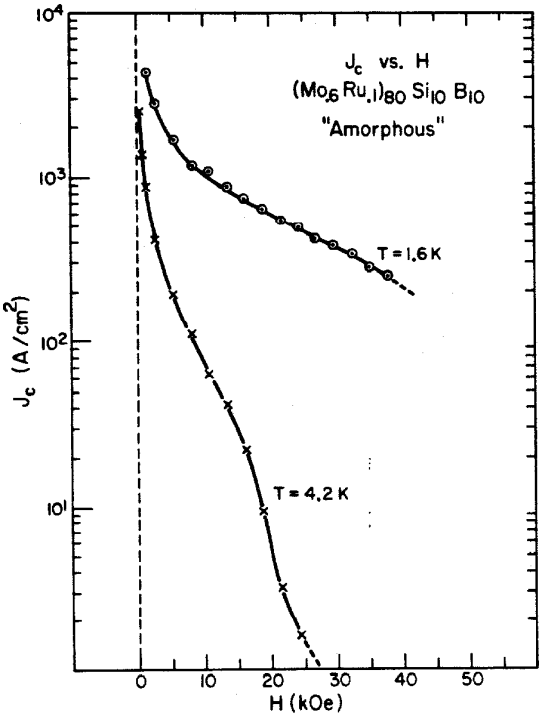

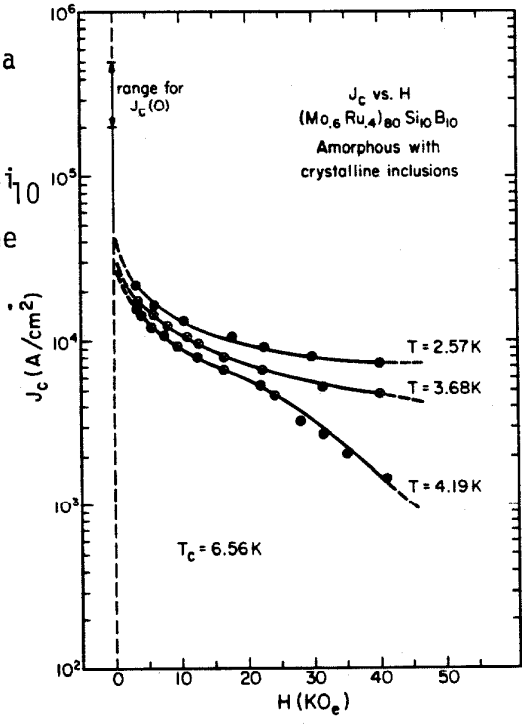

Figure 16. Critical current as a function of applied field for a) amorphous $(Mo_{0.6}Ru_{0.4})_{80}Si_{10}B_{10}$ and b) amorphous plus crystalline inclusions $(Mo_{0.6}Ru_{0.4})_{80}Si_{10}B_{10}$.

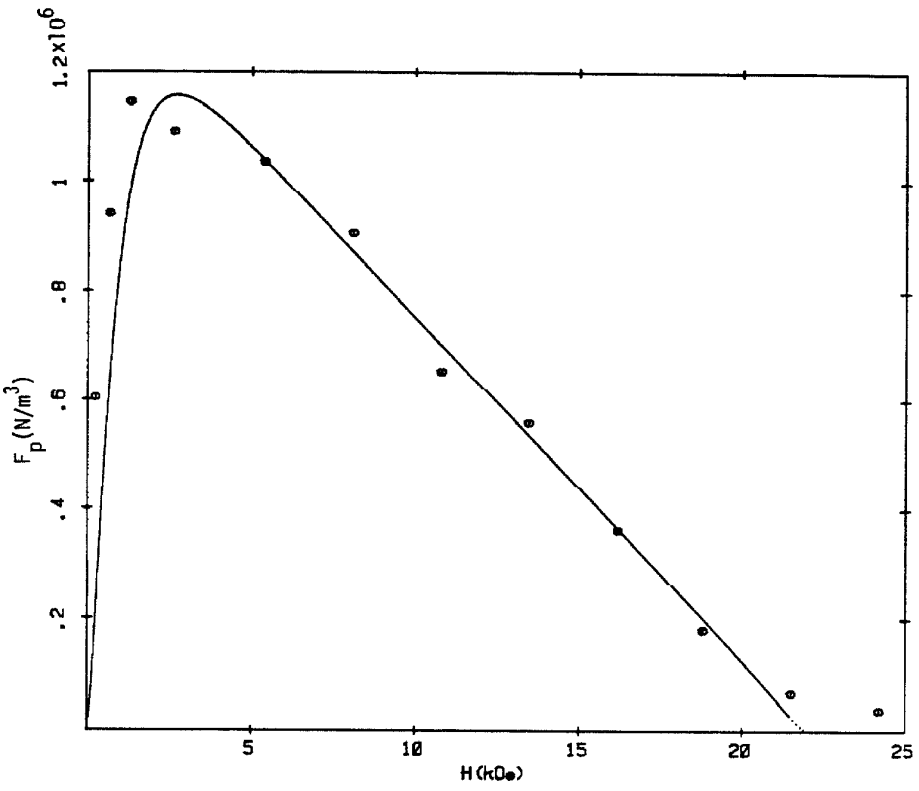

Figure 17. Pinning force as a function of field for amorphous $(Mo_{0.6}Ru_{0.4})_{80}Si_{10}B_{10}$. Also shown is the theoretical result of the dynamic pinning model.

fall off at the fields above the peak. This profile shape is shown in the next section of the thesis to be characteristic of pinning by a surface.

Fig. 18 is the pinning profile for the amorphous plus crystalline sample. In this case the shape is very different from the amorphous sample with the peak occurring at about $H \cong 0.5\ H_{c_2}$. Due to the relatively high critical currents one must use pinning theories in the strong pinning limit to explain this pinning profile shape. A direct summation of the pinning forces, where each flux line interacts with the pinning centers independently of the flux line-flux line interaction and the flux line tension results in $F_p = n\ f_p(h) \propto h^{1/2}(1-h)$. This produces a peak at $h = 1/3$. The dynamic pinning model in the limit of independent flux lines can account for flux line tension and results in $F_p \propto h^{1/2}(1-h)^2$ which peaks at $h = 1/5$. Therefore, neither of these models is successful in accounting for the observed data. The Larkin-Ovchinikov theory in the strong pinning limit finds $F_p \propto h^{5/6}(1-h)^{4/3}$ which peaks at $h = 0.38$. Furthermore, if strong pinning exists, Larkin and Ochinikov find that the flux lines break from the magnetic field lines resulting in $\tilde{C}_{44} = C_{44}(1-h)$. With this modification they find $F_p \propto h^{5/6}(1-h)$. This profile peaks at $h = 0.45$ and as shown in Fig. 18 gives satisfactory agreement with the data.

The scaling law $F_p = CHc_2^n f(p)$ is obeyed in these materials with $n = 2$. Fig. 18 shows the data for three temperatures scaled to the same pinning profile for the sample of amorphous plus crystalline material. The scaling for the purely amorphous material will be discussed in later sections.

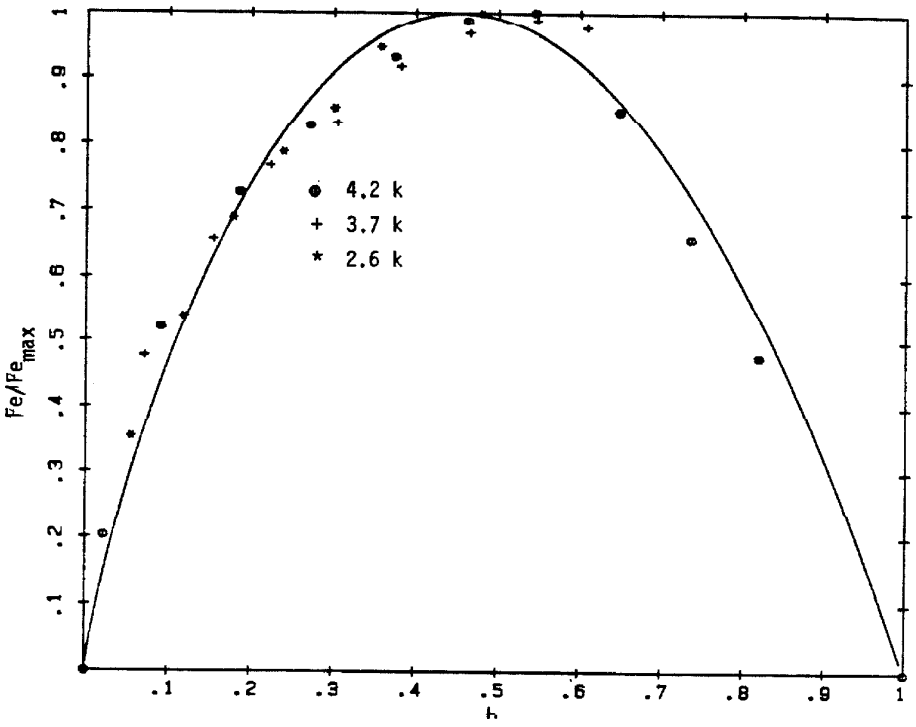

Figure 18. Reduced pinning force as a function of field for amorphous plus crystalline inclusion $(Mo_{0.6}Ru_{0.4})_{80}Si_{10}B_{10}$ at three different temperatures. Also shown is the Larkin-Ovchinnikov strong pinning profile.

In conclusion we can say that the results of these experiments indicate that the characteristic absence of flux pinning in amorphous superconductors can be oversome by the introduction of crystalline inclusions into an otherwise homogeneous matrix. Great differences in the pinning profiles between the amorphous and amorphous plus crystalline sample indicate that two different pinning mechanisms are in effect. The pinning in purely amorphous samples will be analyzed in the next chapter. The amorphous plus crystalline pinning profile is close to the shape predicted by Larkin and Ovchinikov for a large number of randomly spaced medium to strong pinning sites. The crystalline phase inclusions occur in a high density and are randomly spaced. The strength of the pinning interaction should be of medium to high strength since the crystalline inclusion represents an abrupt change in superconducting properties. Thus the pinning mechanism in effect is consistent with the assumptions of the Larkin-Ovchinikov strong pinning theory.

B. Surface Pinning

In the previous section the effect of a rather abrupt inhomogeneity (crystalline inclusions) was investigated. It was shown that the presence of these inhomogeneities drastically affected the critical current. The sensitivity of critical current to the structural state of the material suggests that one may be able to obtain information concerning defects and inhomogeneities in amorphous materials by studying critical current densities. However, in pure amorphous

materials, spatial modulation of the superconducting properties by inhomogeneities and defects on a scale comparable to the superconducting coherence length tends to be small. Thus flux pinning tends to be rather weak in comparison to crystalline materials. Consequently, effects such as sample edge pinning can play an important role in measured critical current density.

In this section we report on measurements of the critical current density in purely amorphous $(Mo_{0.6}Ru_{0.4})_{82}B_{18}$. It was found that flux pinning by the edge of the sample can account for a significant part of the observed critical current. This contribution must be taken into account if a meaningful analysis of flux pinning in amorphous samples is to be achieved.

The samples for this study were prepared by the piston and anvil method described in the experimental section of this thesis. The amorphous nature of the specimens was determined by step scanning on an x-ray diffractometer using Cu Kα radiation. The spectra exhibited the broad smooth bands characteristic of amorphous materials. No evidence of crystallinity was observed in the samples used in this study either by x-ray diffraction or TEM.

Several strips of varying widths (the width, w, is defined as the dimension of the sample perpendicular to both the current and field as shown in Fig. 19) were cut from the same foil with a wire saw. The sample widths were measured with an optical micrometer. The widths ranged from about 0.1 mm to 4 mm. The sample thicknesses were about 40-50 μm.

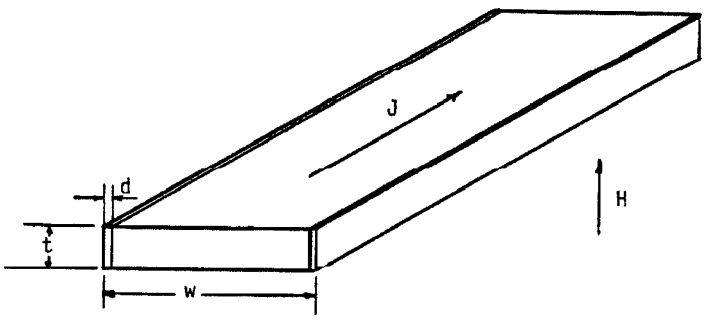

Figure 19. Orientation of critical current sample with respect to field and current.

If pinning is done primarily by the edges of the sample, the flux lines will move unhindered through the bulk of the sample. The volume fraction of strong pinning material will be 2d/w where d is the thickness of the sample region where pinning occurs. (See Fig. 19).

The observed pinning strengths were observed to be very dependent upon sample geometry. The pinning force (F_p) versus field is shown in Fig. 20 for several samples with different widths. The maximum pinning force varies by an order of magnitude with the sample having the smallest width having the highest pinning force. The inset of Fig. 20 shows a plot of F_p versus 1/w for several fields. The linear dependence indicates the presence of edge pinning. The slope of F_p vs 1/w is the force per unit area or pinning pressure on the edges of the sample. Fig. 21 is a plot of the pinning pressure as a function of field found from a least squares fit of pinning force as a function of 1/w. This pinning pressure profile is very similar to the pinning profile found in the previous section for the purely amorphous sample. This suggests that surface edge pinning was dominating the critical current in the prely amorphous sample of $(Mo_{.6}Ru_{.4})_{80}\ Si_{.10}B_{.10}$.

The intercept of the F_p vs 1/w plot gives the width independent of bulk pinning contribution to F_p. The pinning profile obtained in this manner is shown in Fig. 22. Note that this has no peak at low field and the pinning forces are very weak ($\sim 5 \times 10^4 \frac{N}{m^3}$). These pinning forces are so low that they are easily swamped by even relatively weak edge pinning. Precautions such as appropriate sample geometry (large w), the extrapolation technique metnioned above or an A.C. [26]

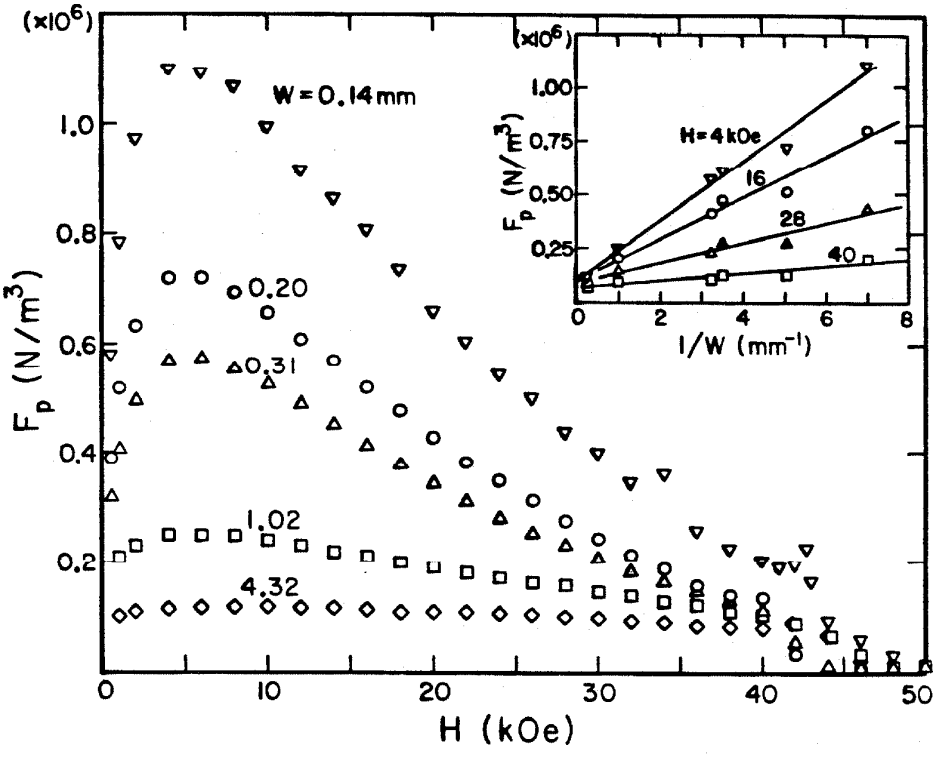

Figure 20. Pinning force versus field for several samples with different widths (dimension of sample measured perpendicular to both current and field). Inset shows linear dependence of pinning force on 1/width.

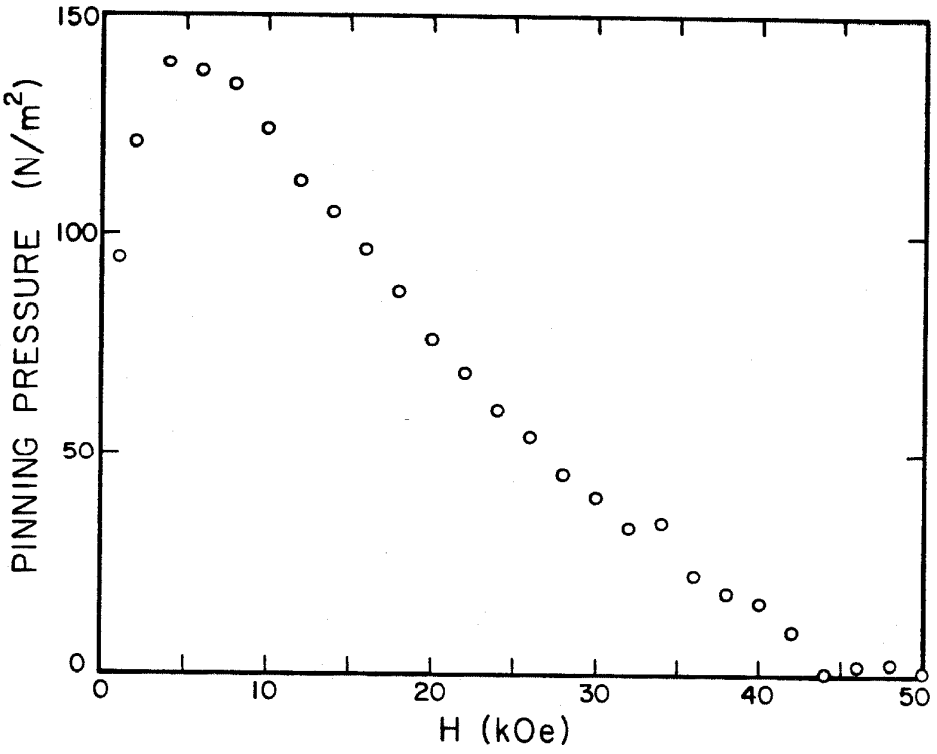

Figure 21, The slope of pinning force vs 1/width (pinning pressure) as a function of field obtained from a least squares fit of pinning force vs 1/width for each value of the field.

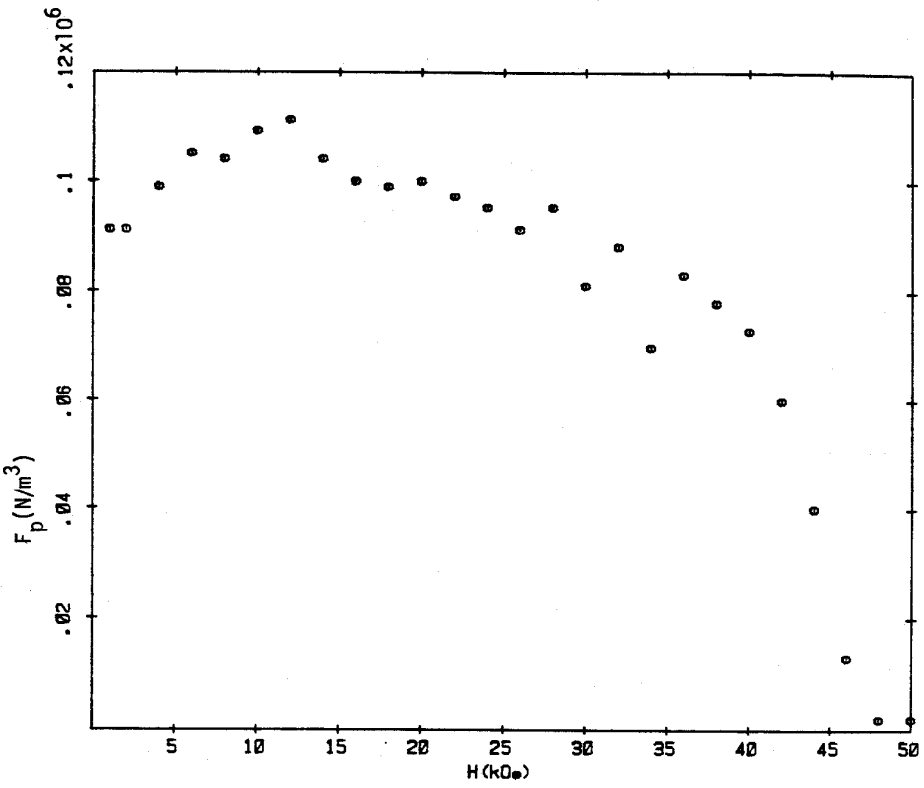

Figure 22. The intercept of pinning force vs 1/width (bulk pinning force) as a function of field obtained from a least squares fit of pinning force vs 1/width for each value of the field.

method which can separate out the surface pinning contribution, must be taken if one is to obtain structural information regarding the bulk material from pinning studies.

In order to gain further insight into the nature of the observed edge pinning force, the samples were electropolished. This treatment removed roughness and irregularities from the edges of the samples. The critical current was dramatically reduced by this treatment. Fig. 23 shows F_p before and after polishing for the narrowest (w=0.14 mm) sample. This sample showed the largest decrease in pinning force upon polishing. The inset shows F_p vs 1/w at an applied field of 16 kG before and after electropolishing. Note the slope is decreased by over an order of magnitude while the intercept is not altered, thus removal of surface irregularities reduced edge pinning and we conclude that surface roughness is the edge pinning mechanism.

Pinning by roughness on the surfaces perpendicular to the magnetic field would produce an increase in pinning force density which is independent of the sample width. Since we observed no change in the intercept of F_p vs 1/w after electropolishing the sample we conclude that roughness on surfaces perpendicular to the magnetic field is not effective in pinning flux within the bulk sample.

The dominant feature of the pinning pressure profile (Fig. 21) is the peak in f_p at low h ($h_p \sim 0.11$) and the near linear fall-off above at fields above h_p. Within the framework of the dynamic pinning model [26,30] there are six possibilities for a peak at low h (see Table I).

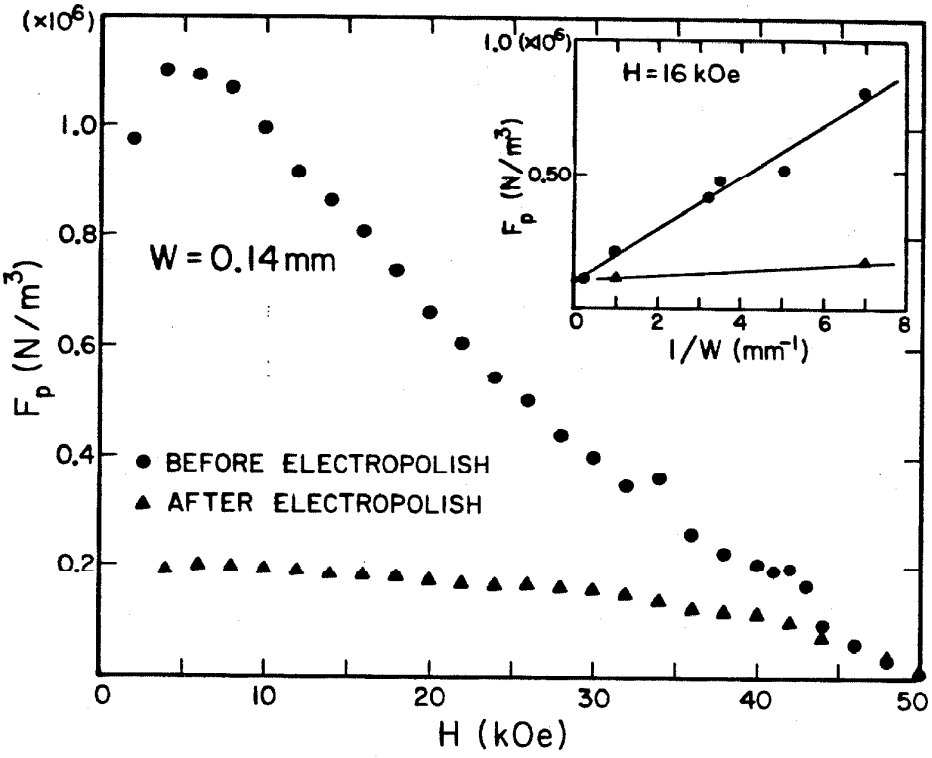

Figure 23. Pinning force as a function of field before and after electropolishing for the narrowest (w = 0.14 mm) sample. Inset shows force as a function of 1/width at an applied field of 16 kG before and after electropolish.

In these cases the pinning force either diverges or is non zero at low h. If we use Kramer's [26] suggestion that the flux lattice shears around the most strongly pinned lines we can produce profiles which peak at low h for all six cases. These are shown in Fig. 24. The profiles in this figure were all constructed assuming the pinning strengths (h) had a distribution $(h) = \frac{1}{2\langle K\rangle} \exp - (K/\langle K\rangle)^{1/2}$ (see Fig. 4 for the effects of varying the pinning strength distribution). The ratio of the shearing force to pin breaking force constants was varied to produce a peak in the generated profiles at the same reduced field as is observed experimentally. The closest agreement to the data comes from a model which assumed $f_p \alpha h^{1/2}(1-h)$ and $C = \sqrt{C_{44}C_{66}}$. The falloff at fields above h_p is linear in this model. Better agreement might be achieved by using a different distribution or a different fitting procedure (e.g., least squares) to determine the ratio of lattice shearing to pin breaking force.

In conclusion, in amorphous superconducting materials where flux pinning is weak, care must be taken in interpretation of critical current measurements. Surface pinning has been shown to dominate the flux pinning profile of such materials and must be eliminated from critical current measurements to yield information on the bulk structure. With these precautions taken, the critical current could now be used as a sensitive probe of the structural state of the bulk material. Application of this method is now demonstrated in the next section of the thesis.

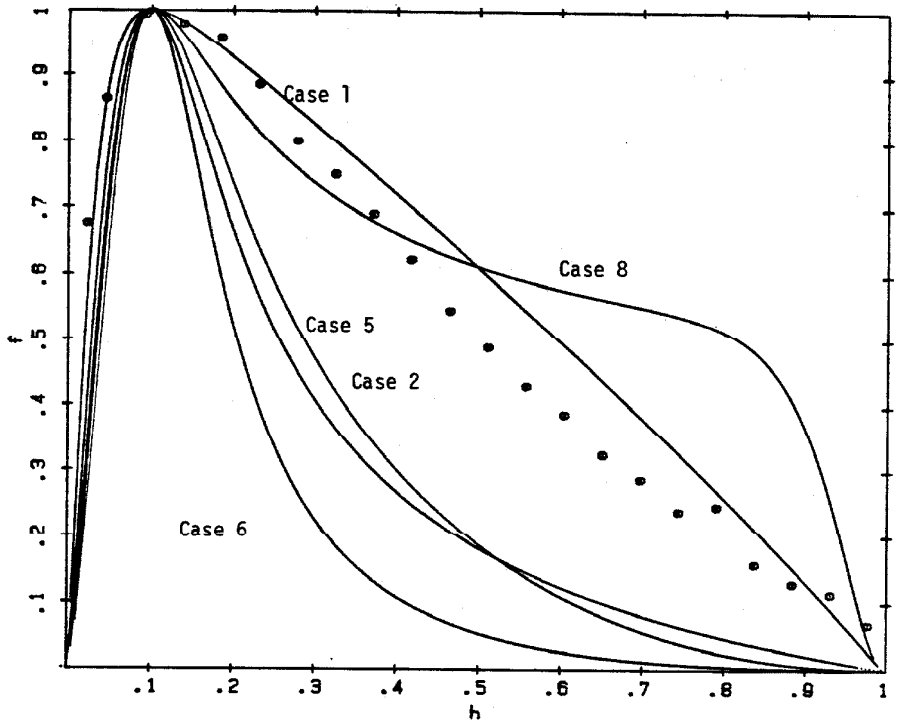

Figure 24. Pinning profiles generated from the dynamic pinning model for the 5 possible cases from Table One for which it is possible to produce a peak at low reduced field.

C. Bulk Flux Pinning Measurements in Purely Amorphous Metallic Glasses

The system $(Mo_{0.6}Ru_{0.4})_{1-x}\ B_x$ can be rapidly quenched to form a glass in the composition range $0.12 \leq x \leq 0.22$, [54] Several properties have been studied as a function of boron content. [41,55] These experiments suggest that there are two types of behavior, corresponding to low and high boron content. For example the electrical resistivity is constant with respect to boron content at low boron content but increases as a function of boron content at high boron content ($x > 0.18$). The electronic density of states $D(\varepsilon_f)$ as found from specific heat shows a step like behavior with low boron content having roughly twice the density of states of the high boron phase. This suggests that there are two structures or phases having respectively, high boron and low boron. These two amorphous phases may each resemble an equilibrium crystalline phase in short range order and composition. For instance, the low boron phase may be similar to σ-MoRu and the high boron phase may resemble boride of Mo or Ru (e.g., Ru_7B_3, Mo_2B). The formation of an amorphous phase in these alloys may be due to competition between two structures as suggested in the discussion on amorphous materials earlier in this thesis.

In this picture, alloys of intermediate composition ($x \sim 0.18$) should be comprised of both types of amorphous phases arranged in a spatial morphology which varies with quench rate and anealling history. If the spatial scale of phase segregation is greater than the superconducting coherence length then the solutions to the Ginsburg-Landau

equations can reflect the presence of two phases. The presence of two phases with different superconducting properties should reflect itself in critical current measurements.

Measurements of resistivity as a function of temperature at high temperatures show that alloys of intermediate composition crystallize in two steps.[56] Fig. 25 shows data for a sample with 18% boron ($x = 0.18$). The two sharp drops in resistivity each represent the transformation of part of the sample to a crystalline phase. Experiments on samples annealed at temperatures below the temperatures required for crystallization suggest that phase separation into two amorphous phases occurs as a precursor to crystallization.[57] Small angle scattering increases after anneals at temperatures above 450° C for times on the order of hours. Embrittlement behavior after annealing also suggests an induced structural change.

In this section critical current measurements on annealed samples with composition $x = 0.18$ show evidence for growth of an inhomogeneity for annealing time and temperature histories which are not observed to produce crystallization. The samples were prepared using the piston and anvil device previously described. The amorphous character of the samples was verified by step scanning x-ray diffraction. The foils were then cut into wide ($w = 0.5$ cm) strips and electropolished to reduce edge pinning effects. The edge pinning contribution was judged to be less than 1%.

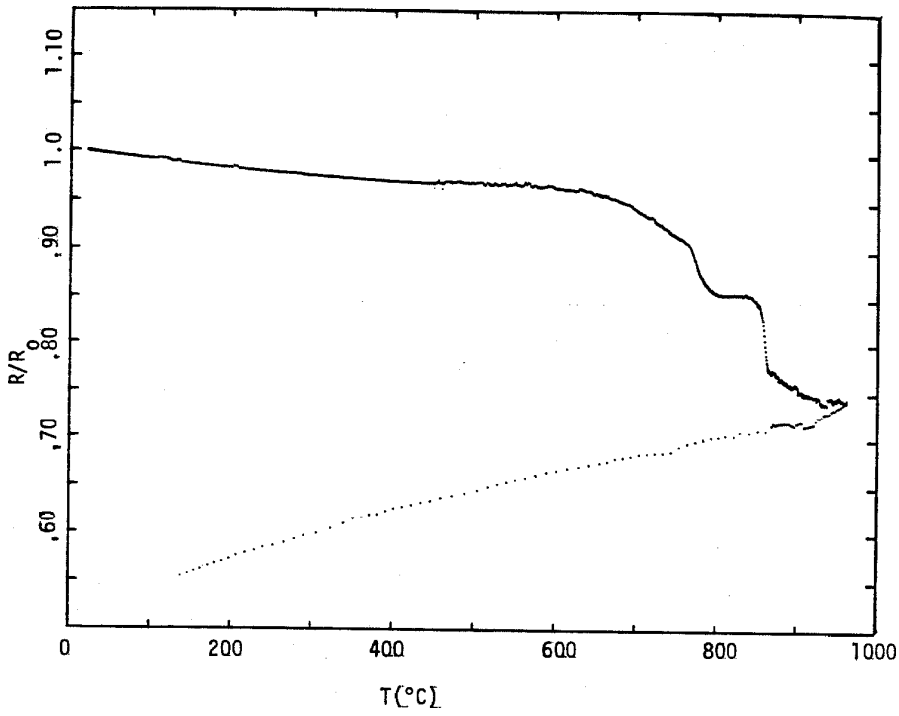

Figure 25. Resistivity as a function of temperature for $(Mo_{0.6}Ru_{0.4})_{82}B_{18}$.

The flux pinning profile for a typical virgin (unannealed) sample is shown in Fig. 26. The profile is characterized by a rapid rise in F_p at low h ($h^{\nu}; \nu \sim 0.5$), an intermediate region where F_p decreases slowly with h and a sharp drop-off near H_{c_2} ($h \sim 1$). These features can be duplicated in a Larkin-Ovchinikov [31] pinning model (Fig. 6). However the profile does not fit the actual data very well as shown in Fig. 26. The data is plotted along with a profile generated with the Larkin Ovchinikov theory where the cross-over between weak pinning and strong pinning is smoothed with a Gaussian distribution of pinning strengths and the cross-over point is chosen to match the peak in F_p in the data.

The as splat samples exhibited a variation in observed pinning force of about 20%. Part of this may have come from inaccuracies in measurement of sample dimensions. However it is clear that samples exhibited a varying amount of inhomogeneities as measured by critical current. The annealing produced changes in T_c and critical fields so the scaling law $F_p \propto H_{c_2}^2 f(h)$ was used to determine a parameter sensitive only to the degree of inhomogeneities and their ability to pin flux is $F_p/H_{c_2}^2$.

Fig. 27 is a plot of $F_p/H_{c_2}^2$ for a sample annealed at 550° C for several different annealing times. Note that the effect of an anneal is to first lower and then increase the pinning force. This behavior is also shown in Fig. 28 for two different annealing temperatures, where we have plotted $F_p/H_{c_2}^2 / F_p/H_{c_2}^2$ for two different samples
virgin

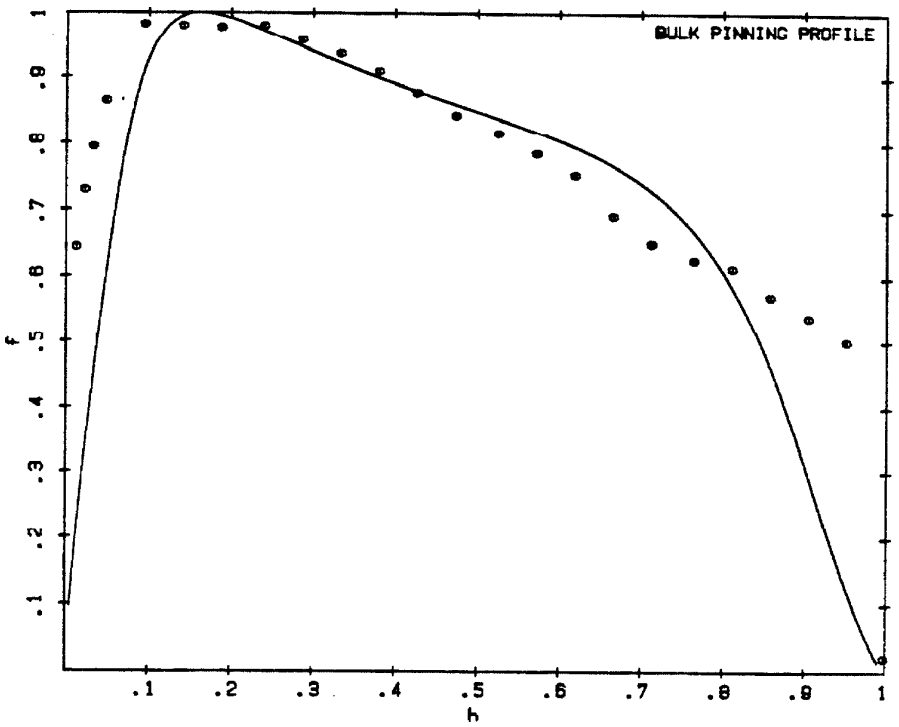

Figure 26. Pinning profile for $(Mo_{0.6}Ru_{0.4})_{82}B_{18}$ in unannealed condition. Also shown is pinning profile generated from the Larkin-Ovchinnikov pinning theory.

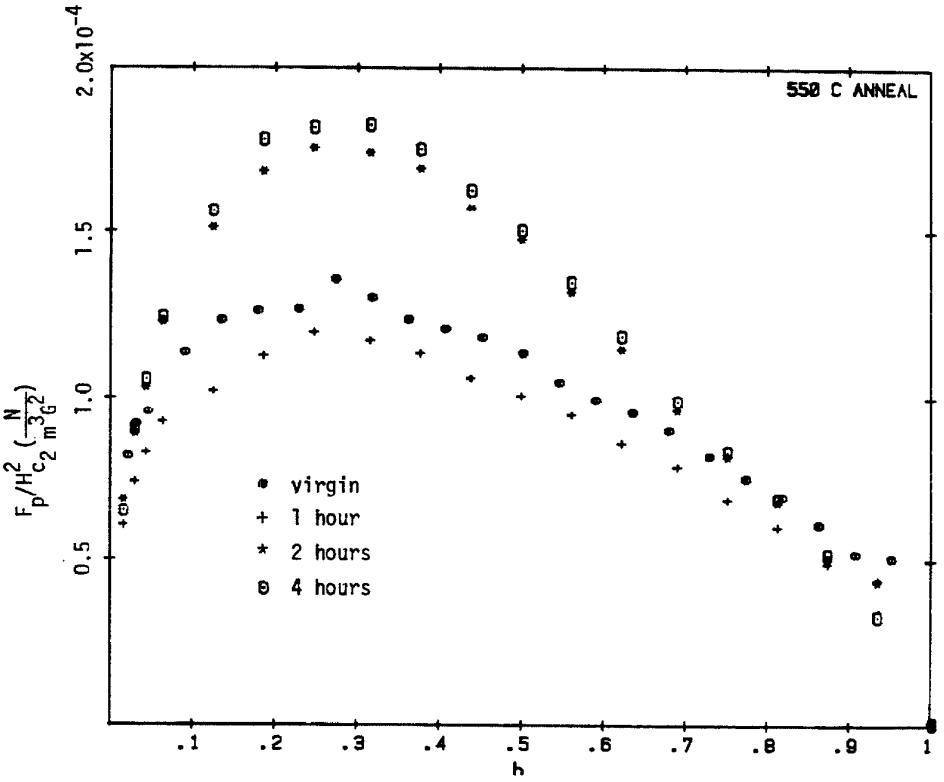

Figure 27. Pinning force parameter $F_p/H_{c_2}^2$ plotted versus reduced field for a sample of $(Mo_{0.6}Ru_{0.4})_{82}B_{18}$ annealed at 550° C for different amounts of time.

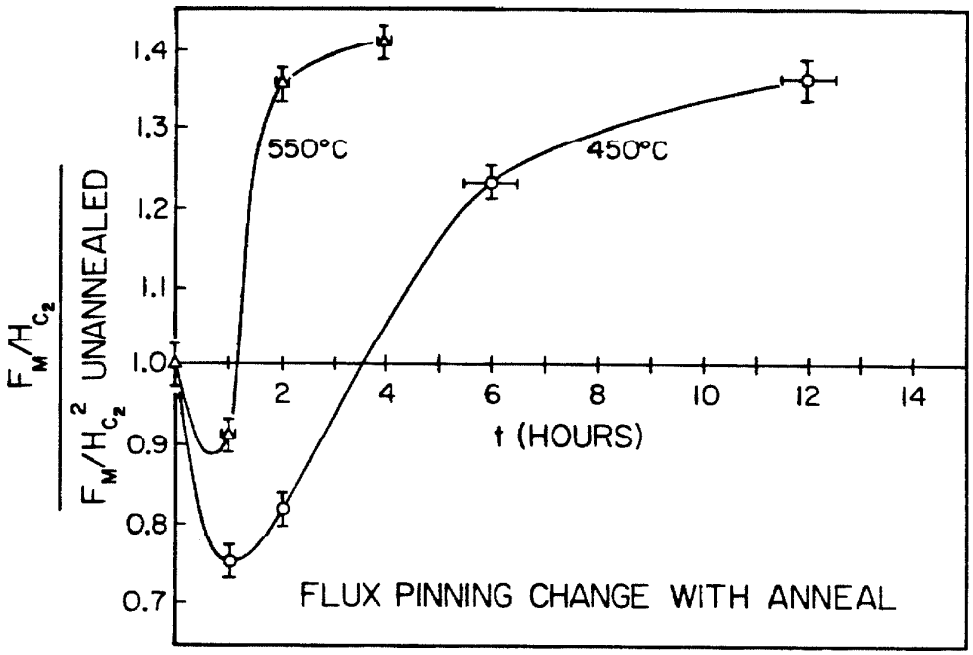

Figure 28. Pinning force change plotted as a function of time for samples of $(Mo_{0.6}Ru_{0.4})_{82}B_{18}$ given consecutive anneals at a given temperature. Results are shown for samples annealed at 450° C and 550° C.

annealed for varying times. We see that the pinning force changes on two different time scales, first a fairly rapid decrease followed by a slower increase.

The critical temperature, T_c, is shown in Fig. 29 where we plot the change in this property as a function of annealing time. In contrast to the pinning force, T_c only responds to an anneal in one manner, decreasing following the time scale of the decrease in pinning force.

The decline in T_c has been observed in amorphous materials.[58] Similarly, the magnetic coercive force in amorphous ferromagnetic materials has been observed to drop following relatively mild anneals.[59] This behavior has been attributed to relaxation of quenched in strains. This relaxation process involves only atomic motions over small distances (distances less than nearest neighbor spacings). The excess volume defects are observed to vanish as the atomic density increases.[58] The initial decrease in flux pinning force following an anneal is thus most likely due to the relaxation of quenched inhomogeneous strains.

The increase in flux pinning following subsequent anneals is evidence for growth of an inhomogeneity in superconducting properties. This inhomogeneity may be a compositional segregation occurring as a precursor to crystallization, such as spinodal decomposition discussed in an earlier section of this thesis. If this inhomogeneity is segregation into boron rich and boron poor amorphous phases, the formation of these regions will involve movement of boron atoms over several

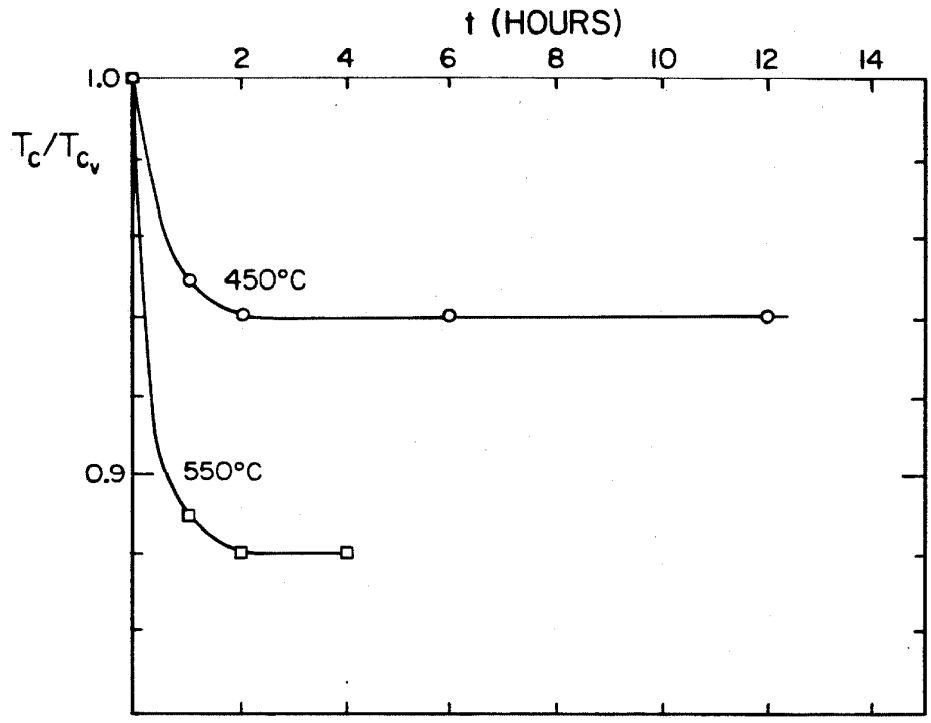

Figure 29. Change in superconducting transition temperature plotted as a function of time for samples of $(Mo_{0.6}Ru_{0.4})_{82}B_{18}$ given consecutive anneals at a given temperature. Results are shown for samples annealed at 450° C and 550° C.

atomic distances. An activation energy for this process can be estimated from the data to be about 0.5 eV. This is consistent with the interpretation that this is a compositional segregation involving the diffusion of boron. [38]

Considerable evidence for phase separation in metallic glasses upon annealing has been presented in the literature. Fluctuations in metaloid content do not produce a large difference in electron density making these inhomogeneities impossible to unambiguously observe with transmission electron microscopy. Therefore much work has been done with small angle x-ray scattering (SAXS) to observe and characterize decomposition into two amorphous phases. Walter, Le Grand and Luborsky [60] have used Auger analysis in conjunction with SAXS to observe phosphorous rich regions which increase in number upon annealing in the metallic glass $Fe_{40}Ni_{40}P_{14}B_6$. SAXS has also been used to observe growth of inhomogeneities in Fe-B, Fe-P-C and Pd-Au-Si glasses. [61] Piller and Haaser [42] have used atom probe field ion microscopy to observe decomposition of amorphous $Fe_{40}Ni_{40}B_{20}$ into two amorphous phases, of composition $(FeNi)_3B$ and a solid solution FeNiB of lower boron content. The formation of a phase with the stoichiometry of a crystalline compound $(FeNi)_3B$ suggests that this process is a precursor to crystallization. The size of the inhomogeneities observed in these experiments varies from 10 to 60 Å.

Koch et al [57] have studied SAXS in $(Mo_{0.6}Ru_{0.4})_{82}B_{18}$. They found three regions in time-temperature behavior. At low temperatures and short times (e.g., 500° C 1 hour) only small decreases in SAXS

Intensity were observed. This corresponds to the relaxation observed in T_c and decrease observed in pinning force. At higher temperatures (e.g., 550° C 1 hour) SAXS intensity was observed to increase due to inhomogeneities with a characteristic dimension of about 80 Å. This suggests a phase separation similar to that observed by Piller and Haasen. The two amorphous phases in this case may be related to the σ-MoRu and the borides of Mo and Ru (Mo_2B Ru_7B_3). This increase in SAXS intensity reflects the presence of the inhomogeneities which may be responsible for the increase in J_c observed in our experiments. The third region in SAXS behavior is at high temperatures or long times (e.g., 550° C 500 hours) is characterized by formation of a large number of small (50-100 Å) crystallites. This region was never reached in our experiments.

In conclusion, the annealing of glass $(Mo_{0.6}Ru_{0.4})_{82}B_{18}$ produced two effects in the flux pinning strengths. First a decrease occurs in the flux pinning strength parameter ($F_p/H_{c_2}^2$). This is interpreted as resulting from annealing out of quenched in inhomogeneous strain fields on excess volume defects. The second effect was an increase in pinning force. This is due to a growth in an inhomogeneity which may be a compositional segregation such as the spinodal decomposition into boron rich and boron poor phases which act as a precursor to crystallization. Thus critical current can be used as a probe to sense inhomogeneities which are difficult or impossible to observe with other methods.

D. H_{c_2} Measurements

The upper critical field curves of amorphous superconduction alloys has recently been the subject of much discussion. Amorphous superconductors exhibit a variety of upper critical field (H_{c_2}) behaviors. In the amorphous $Cu_{1-x}Z_{Cx}$ [62] system the upper critical field vs temperature ($H_{c_2}(T)$) curves follow the theory of Werthhamer, Hefland and Hoherberg (WHH). [23] However, in amorphous MoRu-based alloy systems, the upper critical field exhibits an extended linear region. [53,63] Carter et al [64] have shown from a phenomenological modification of the Maki equation that a distribution of electric diffusivities results in enhanced critical fields. This leads to the postulation that inhomogeneities may be the cause of this extended linear region, This supposition in combination with the observation that annealing produced inhomogeneities in amorphous $(Mo_{0,6}Ru_{0.4})_{82}B_{18}$ as reflected in small angle x-ray scattering (SAXS) [57] and flux pinning measurements, was motivation for the investigation of the $H_{c_2}(T)$ curves for annealed $(Mo_{0,6}Ru_{0,4})_{1-x}B_x$ alloys.

Upper critical fields were measured using the standard four point probe method at the Francis Bitter National Magnet Laboratory for amorphous $(Mo_{0,6}Ru_{0,4})_{1-x}B_x$ samples with x = 0,14, 0,18 and 0,22. Samples from the same foil for each composition were measured in the as quenched and annealed (2 hours 525° C) condition. The samples were examined before and after anneal by step scanning x-ray

diffraction. No evidence for crystallinity was observed in any samples used in this study. Snall angle x-ray scattering measurements were performed at Oak Ridge National Laboratory prior to being cut into strips for the H_{c_2} (T) measurements.

Table 5 summarizes the effects of the thermal anneal on the SAXS and superconducting measurements. The SAXS plotted as a function of scattering vector (k) approach a maximum at small k for each of the samples. This maximum, in units of scattering events per second per cubic centimeter is the value reported in Table 5. The SAXS for each composition increased after an anneal, suggesting that annealing produced inhomogeneities in the samples. The critical temperature was lowered for the x = 0.14 and x = 0.18 samples. This is consistent with the annealing effects on T_c reported in the previous section of this thesis. The T_c for the x = 0.22 sample increased upon annealing, this behavior in conjunction with the dramatic increase in SAXS as a result of the anneal suggests that a significant growth of a high T_c phase occurred during anneal. The transition width (ΔH_{c_2}) is also listed in Table 5. The transition width for each composition increased upon anneal. This implies that a broadening in the dsitribution in superconducting properties within the sample is produced by the anneal. This agrees with the conclusion drawn from the SAXS measurements which is that inhomogeneities are produced by the anneal. The inhomogeneities produced are most probably of the same nature as those observed in the flux pinning measurements of annealed samples as reported in the previous

X	Anneal	SAXS $(\frac{\text{events}}{\text{cm}^3\text{sec}})$	T_c(K)	$\frac{dH_{c_2}}{dT}T_c$ $(\frac{kG}{K})$	ΔH_{c_2} (kG)
0.14	as quenched	$2x10^3$	6.63	23.7	2.7
0.14	2 Hr 525°C	$4.8x10^3$	6.48	26.2	7.5
0.18	as quenched	$3.2x10^3$	6.21	24.5	5.4
0.18	2 Hr 525°C	$6.2x10^3$	6.03	24.0	8.8
0.22	as quenched	$2x10^2$	5.13	25.5	5.5
0.22	2 Hr 525°C	$2.5x10^3$	5.74	∿29	16.5

TABLE 4. Composition, condition, small angle x-ray scattering, transition temperatures, critical field gradient, and transition widths for $(Mo_{0.6}Ru_{0.4})_{1-x}B_x$ samples.

section of this thesis. As we suggested there, this inhomogeneity may be a compositional segregation which occurs as a precursor to crystallization of boron rich and boron poor phases.

The effect of the anneal on the upper critical field curves for each composition was to cause a decrease in the extended linear region. This is seen most dramatically for the x = 0.22 sample as shown in Fig. 30 where the $H_{c_2}(T)$ is plotted for the before and after anneal samples. Also plotted is the Maki [22] curve which is the WHH [23] result in the limit of infinite spin orbit coupling. This is the highest $H_{c_2}(T)$ which can be derived from the WHH theory. The $H_{c_2}(T)$ for the unannealed sample lies above even that for this non-physical limit of the theory, as is typical of all the unannealed samples measured in this study. The effect of the anneal was to drop the $H_{c_2}(T)$ below the Maki curve as shown in Fig. 30. This reduction in the extended linear region of $H_{c_2}(T)$ curves occurred upon annealing to a lesser extent in the x = 0.14 and x = 0.18 samples. If the extended linear region is due to inhomogeneities, then we would have expected the $H_{c_2}(T)$ curves to become more linear upon annealing. The observation of the opposite effect implies that inhomogeneities, at least those of the type grown during an anneal are not responsible for the enhanced upper critical fields.

The $H_{c_2}(T)$ curve for the annealed x = 0.22 sample shown in Fig. 30 shows a greater downward curvature near T_c than the $H_{c_2}(T)$ curve for the unannealed sample. One possible explanation for an inhomogeneous sample exhibiting this behavior lies in the coherence length dependence on T. The coherence

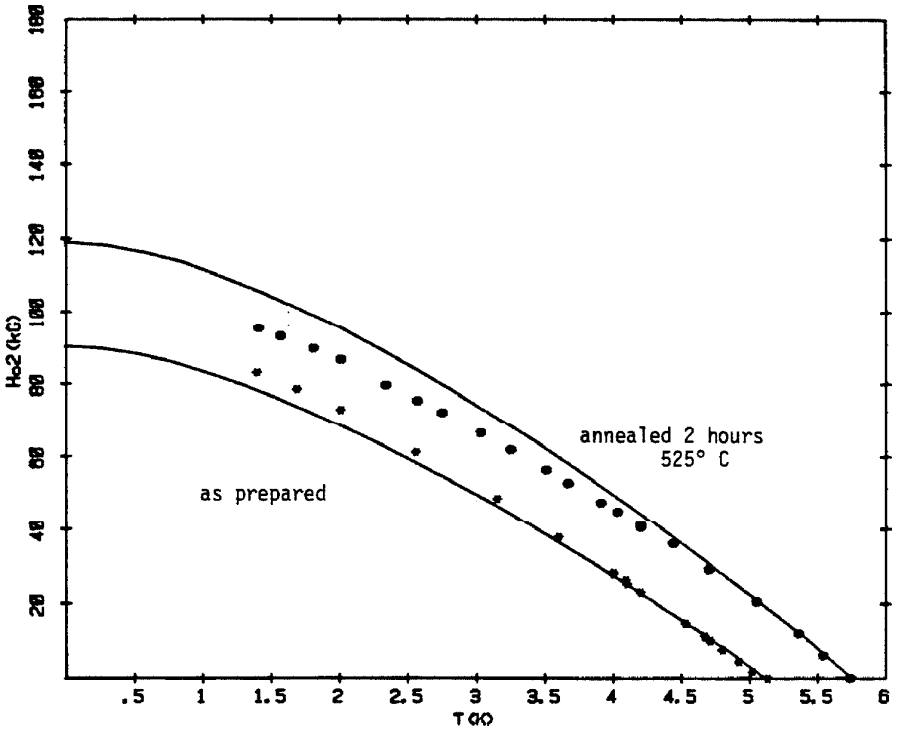

Figure 30. Upper critical field versus temperature for samples of $(Mo_{0.6}Ru_{0.4})_{78}B_{22}$ before and after annealing for two hours at 525° C.

length ξ depends on T as $(1-T/T_c)^{-1/2}$. At low temperatures ($T << T_c$) the coherence length is small and solutions to the Ginsburg-Landau equations can exhibit spatial variations which reflect the presence of inhomogeneities. The $H_{c_2}(T)$ behavior will then be dominated by high H_{c_2} high T_c regions. As T approaches T_c the coherence length diverges and thus at some temperature the coherence length will become larger than the spatial dimensions of the high T_c high H_{c_2} regions. The solution to the Ginsburg-Landau equation will then reflect an average of the superconducting properties within the volume ξ^3. The inability of the superconducting state to reflect the properties of the high H_{c_2} high T_c inhomogeneities will cause a downward curvature in $H_{c_2}(T)$ near T_c.

In conclusion we have demonstrated that following an anneal of 2 hours at 525° C samples of $(Mo_{0.6}Ru_{0.4})_{1-x}B_x$ with x = 0.14, 0.18 and 0.22 become more inhomogeneous as indicated by SAXS and critical field transition width behavior. The attempt to demonstrate that the enhanced upper critical field characteristic of Mo Ru based amorphous superconductors is a direct result of inhomogeneities failed. In fact we observed that the annealed samples exhibited greater downward curvature in $H_{c_2}(T)$ curves than the more homogeneous unannealed samples. This behavior is interpreted as being the result of the superconducting coherence length becoming larger than the spatial dimensions of the high H_{c_2} high T_c regions of the sample.

V. Measurements on Sputter Deposited and Ion Beam Mixed Films

A. Sputter Deposition

The relationship between amorphous structures produced by rapid quenching from the melt and those produced by methods which involve solification from the vapor phase such as sputter deposition has been the subject of much study. [65, 66, 67] The relationship between the liquid phase and the liquid quenched amorphous phase is obviously direct. Structures, defects and inhomogeneities which are present in the liquid phase are likely to occur in the liquid quenched material. Vapor deposition, on the other hand, allows for atomic arrangements which are not related to the liquid structure. Defects such as excess volume and density fluctuations occur more often in vapor quenched materials. [65, 66] Gaseous impurities present in the vapor deposition environment are often trapped in the deposited foil, often helping to stabilize the amorphous phase. [65, 68] The structural comparison in x-ray defraction generally shows that the vapor deposited structures are more loosely packed with a greater nearest neighbor distance than a corresponding liquid quenched material. [65] The main features of the structure remain the same for materials prepared by both techniques. The broad bands and split second maxima in the x-ray diffraction pattern are common to both materials. [65, 66]

In the present study samples of composition $(Mo_{0.6}Ru_{0.4})_{82}B_{18}$ were prepared by sputter deposition as described previously and

compared with liquid quenched alloys of the same nominal composition. The comparison of the superconducting properties, in particular critical current, revealed considerable differences between the two structures. The sputtering environment was varied by increasing the pressure of argon gas in the deposition chamber. This proved to have dramatic effects on the superconducting properties of the material. The effect of thermal anneals on the superconducting properties of the sputtered material was investigated.

Table five summarizes the results of the critical temperature and critical field measurements performed in this study. Note that the as sputtered sample prepared in 5 μm argon pressure has a T_c (T_c = 6.91k) which is higher than the T_c for the melt quenched material (T_c = 6.05k). After annealing (500° C 20 hours) the T_c lowers to a value closer to the liquid quenched material. The material sputtered under 75 μm Ar pressure has a lower T_c (T_c=3.85k) which is increased by an anneal to T_c = 5.12 k. In both these cases (Ar pressure = 5 μm and 75 μm) these measurements imply the presence of a defect or structure which is present to a greater degree in the sputtered film than the liquid quenched alloy, but which decreases upon annealing. In the case of the material sputtered in 5 μm Ar pressure it is likely that the mechanism which decreases T_c upon annealing is similar to that which decreases T_c upon annealing in the liquid quenched alloys. This implies that the sputtered materials have a greater amount of quenched in strains or excess volume than liquid quenched alloys. This is not surprising since

Preparation Conditions	T_c	$\left.\frac{dH_{c_2}}{dT}\right\|_{T_c}$ $(\frac{kOe}{K})$	$\Delta H(kOe)$
5 μm Ar pressure as sputtered	6.9	24.7	6.5
5 μm Ar pressure annealed 500°C, 20 hours	6.3	25.8	7.4
75 μm Ar pressure as sputtered	3.85	44.4	14
75 μm Ar pressure annealed 500°C, 20 hours	5.12	70.3	46

TABLE 5. Preparation conditions, transition temperature, critical field gradients, and transition widths for samples of sputtered $(Mo_{0.6}Ru_{0.4})_{82}B_{18}$.

sputtering produces a rapid quench from a more highly disordered phase than does a liquid quench.

The critical field gradient $\left.\frac{H_{c_2}}{dT}\right|_{T_c}$ for the low Ar pressure as sputtered film is about the same as that of the liquid quenched material. Upon annealing the critical field curve (Fig. 31) shows an upward kink which can be interpreted as evidence for a two phase material, one phase having a lower T_c and higher critical field gradient than the other. The sample sputtered in high Ar pressure has extremely high upper critical field gradients both before and after annealing (Table 4). The resistive transition is also very broad (40 kG) before and after annealing. This suggests a very inhomogeneous material.

The flux pinning force versus field for the as sputtered in low Ar pressure sample is shown in Fig. 32. The most marked feature is a relatively sharp peak near H_{c_2}. This is not present in the liquid quenched material. This so-called peak effect has been observed in many materials, including amorphous sputtered Nb_3Ge [69] and liquid quenched LaAlGd alloys. [70] In the case of the LaAlGd alloys the height and width of the peak was found to be proportional to the Gd content, leading to the speculation that it is fluctuations in the Gd content which act as pinning sites. Gd carries a magnetic moment ($\sim 7\ \mu_B$) which can interact with a flux vortex. These would be weak randomly arranged pinning centers and thus one would expect that a Larkin-Ovchiniknov collective pinning model would apply.

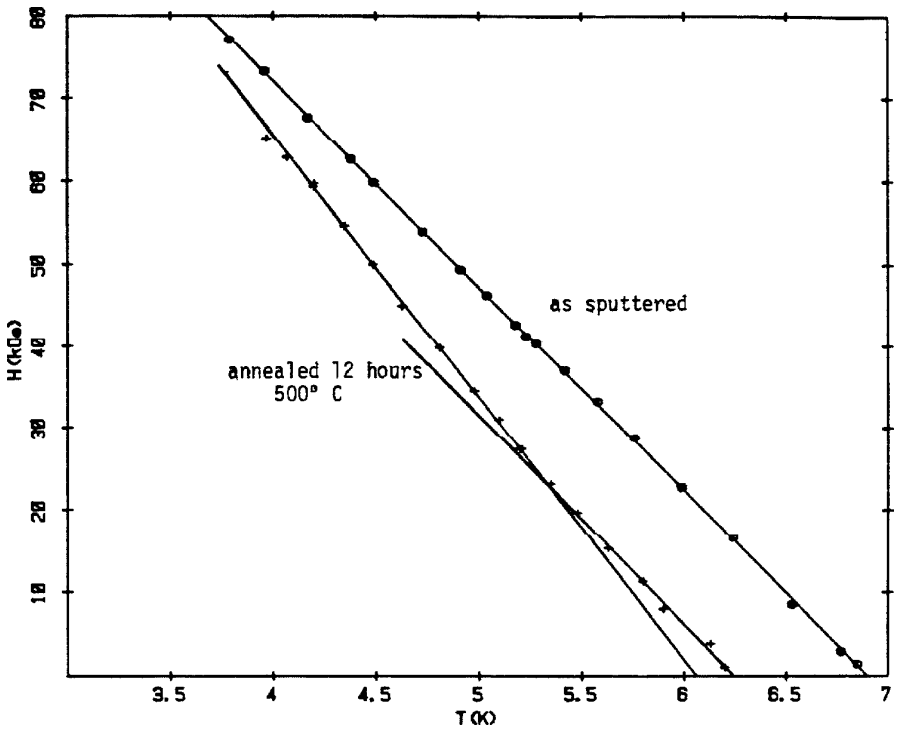

Figure 31. Upper critical field versus temperature for sputtered $(Mo_{0.6}Ru_{0.4})_{82}B_{18}$ before and after annealing for 12 hours at 500° C.

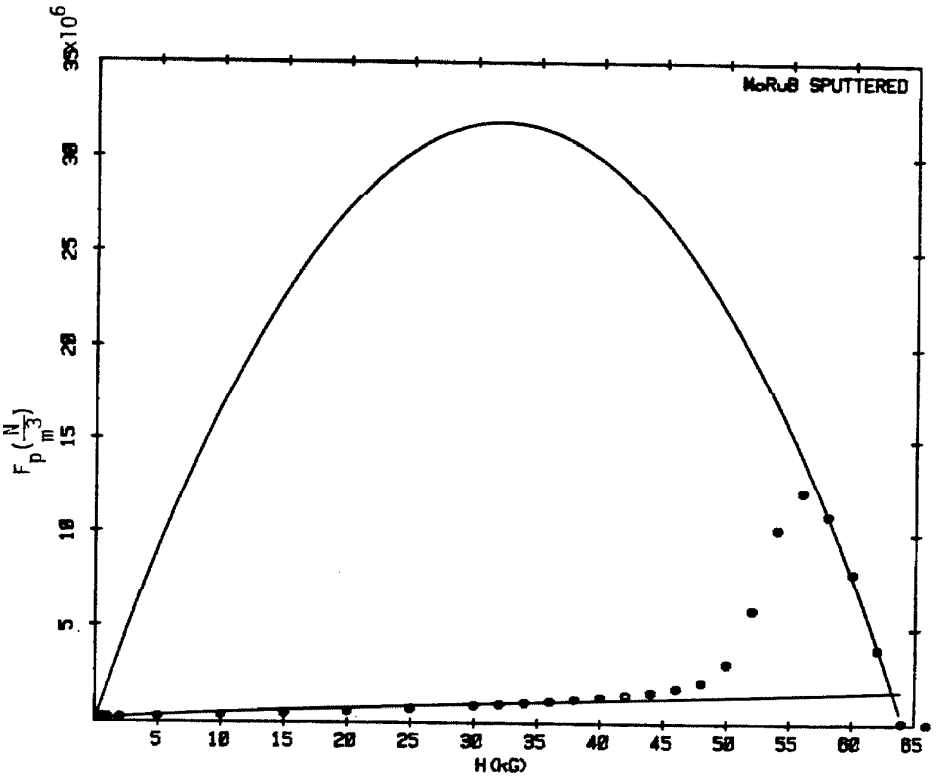

Figure 32. Pinning force versus field for $(Mo_{0.6}Ru_{0.4})_{82}B_{18}$ sputtered in 5 μM Ar pressure. Also shown is fits to the data from the two dimensional strong pinning and weak pinning Larkin-Ovchinnikov collective pinning model.

Kes and Tseui [69] have argued that in the case of amorphous sputters Nb_3Ge films, the peak effect was caused by a pinning mediated disorder in the flux line lattice. They have argued that in the case of thin films, the radius of curvature of the flux lines is much greater than the thickness of the film so a two dimensional pinning model will apply. Within the framework of the Larkin-Ovchinikov model this implies that the volume of coherent flux lines V_c becomes $V_c = R_c t$ where t is the thickness of the film. This leads to the expression for the flux pinning force $F_p \propto \frac{N_v f_p}{a_o d C_{66}}$ which is independent of the bending modulus C_{44} and has the field dependence $F_p \propto \frac{h^{1/2}}{1-0.29h}$. If the pinning becomes strong the distance over which the flux lines remain coherent (R_c) approaches the flux line lattice spacing. This leads to the strong field dependence $F_p \propto h(1-h)$. In the present case the pinning force at low fields follows the weak pinning field dependence. However, as field increases, the Kes and Tseui pinning mediated disorder in the flux line lattice results in a decrease in C_{66}, causing an increase in pinning force. As C_{66} decreases, the R_c approaches a_o and the pinning force decreases with field with the strong pinning field dependence. Fig. 32 shows the pinning profile for the as sputtered in low Ar pressure sample plotted with the weak pinning profile fitted to the low field data and the strong pinning profile fitted to the high field data. The relative ratio of the strong to weak pinning profile fits are consistent with the value calculated from the theory,

The high field fall off of F_p can be extrapolated to find the upper critical field. This value (which we will refer to as $H_{c_{2_p}}$) can be compared to that measured by the conventional method described earlier in this thesis (which we shall refer to as $H_{c_{2_R}}$). The value determined from extrapolation of flux pinning measurements is representative of the bulk of the sample while the conventional method only determines the point at which a super current can percolate through the sample. Percolation at a supercurrent only requires that one continuous path be superconducting which requires that about 15% of the sample be superconducting.[71] If there exists within the sample a distribution of superconducting properties then $H_{c_{2_R}}$ will be greater than $H_{c_{2_p}}$ by an amount which reflects the width of the distribution of superconducting properties.

Samples which were sputtered in 5 μm Ar pressure were annealed at 500° C for 12 and 20 hours. Fig. 33 shows the pinning force parameter $F_p/H_{c_2}^2$ versus reduced field $H/H_{c_{2_R}}$ for the virgin and annealed samples. Note that the amplitude of the peak first decreases then increases in a manner similar to annealed liquid quenched material. Also note that the peak shifts to lower field following progressive anneals which reflects the fact that $H_{c_{2_p}}$ drops relative to $H_{c_{2_R}}$. This suggests that the range of superconducting properties which exist in the sample is increased by annealing. This agrees with the conclusions from the H_{c_2} measurements, which also suggested a range of superconducting properties occurring after an anneal.

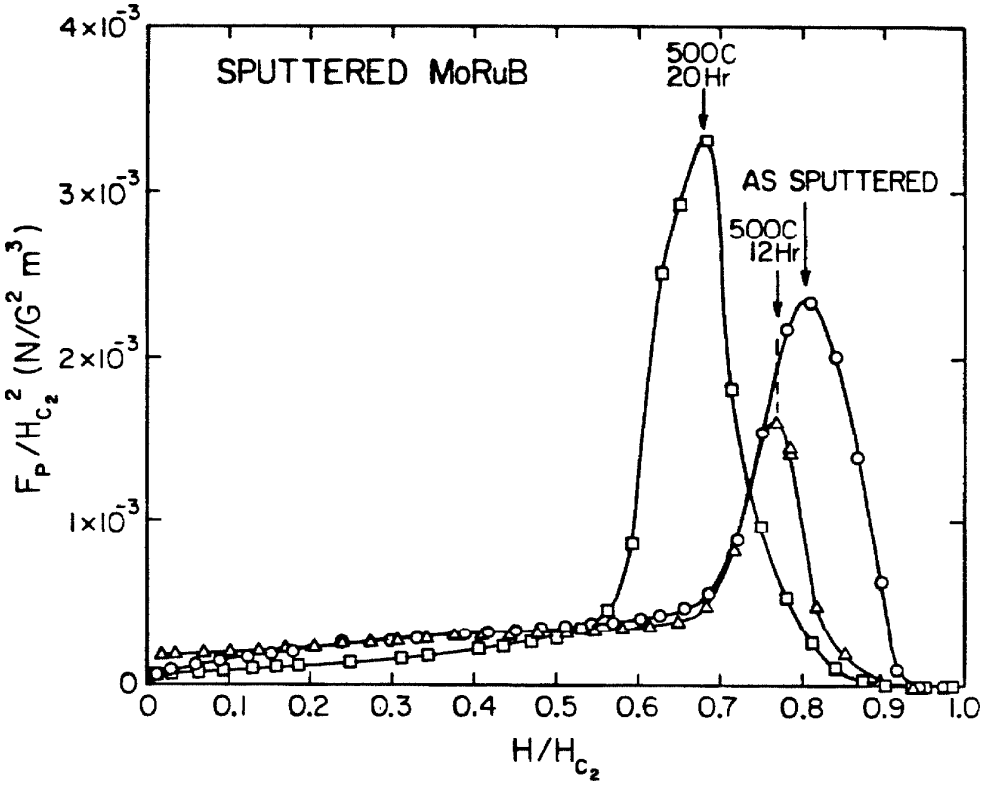

Figure 33. Pinning force parameter $F_p/H_{c_2}^2$ versus reduced field for $(Mo_{0.6}Ru_{0.4})_{82}B_{18}$ sputtered in 5 μm Ar pressure before and after anneals of 12 and 20 hours at 500° C. Solid line is a visualization aid.

The nature of the inhomogeneities occurring after a thermal anneal in the sputtered materials studied here is probably similar to the inhomogeneities which occurred upon annealing the liquid quenched material of the same composition. The driving mechanism for composition segregation will be the same in both cases and compositional segregation must occur for the material to crystallize. Thus the changes in flux pinning force and critical field is evidence for phase separation in annealed sputtered films.

The sample which was sputtered in 75 μm of Ar pressure exhibited a very different pinning profile from the sample sputtered in 5 μm Ar pressure. Fig. 34 shows the pinning force parameter $F_p/H_{c_2}^2$ versus reduced field $H/H_{c_{2_R}}$ for both samples. The high Ar pressure results in a big difference between $H_{c_{2_R}}$ and $H_{c_{2_p}}$ which indicates a broad distribution of superconducting properties. At fields below $H_{c_{2_p}}$ the pinning profile exhibits one broad smooth maxima which is characteristic of strong pinning mechanisms. Transmission electron microscopy [72] performed on samples deposited under the same conditions (high Ar pressure) showed a structure formed of clusters of relatively dense material connected by less dense material. This is similar to the cluster formation observed in Aℓ-$Aℓ_2O_3$ films. [73] The flux pinning data in combination with the very wide transition width observed in H_{c_2} measurements indicate that the material deposited under 75 μm Ar pressure is very inhomogeneous in an as sputtered condition. This inhomogeneity is likely due to clustering during deposition.

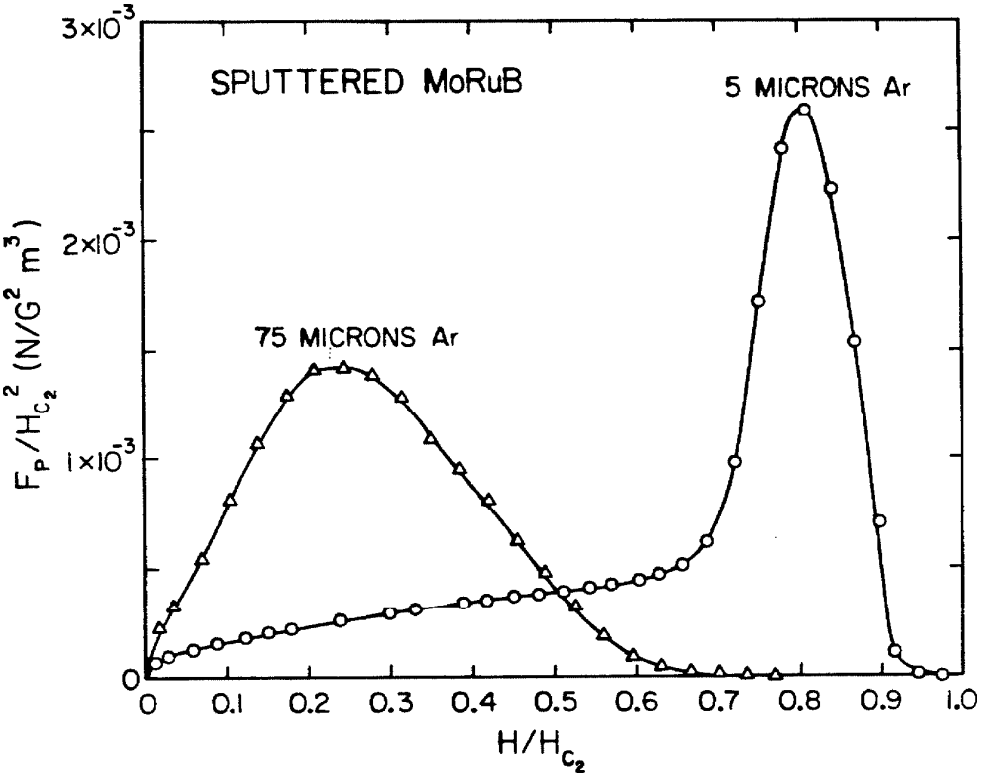

Figure 34. Pinning force parameter $F_p/H_{c_2}^2$ versus reduced field for $(Mo_{0.6}Ru_{0.4})_{82}B_{18}$ sputtered in 5 μm and 75 μm Ar pressure.

In conclusion sputter deposition in low Ar pressure produced material which exhibits many of the properties of liquid quenched material. Quenched in strains or excess volume seem to be present in a greater degree than in liquid quenched materials as evidenced by the larger drop in T_c upon annealing. Evidence for phase separation upon annealing is observed in flux pinning measurements performed on samples prepared by both methods. A peak in the flux pinning profile which occurs in the sputtered materials is thought to be attributable to an intrinsic inhomogeneity which occurs in sputtered materials but not in liquid quenched materials but may be due to the two dimensional character of the flux pinning in the thinner sputtered materials. Sputter deposition in higher Ar pressure (75 μm) produced very inhomogeneous materials as evidenced by T.E.M., flux pinning profile and H_{c_2} measurements.

B. Ion Beam Mixed Films

Ion beam mixing is a novel method for preparation of metastable structures.[74] This method, as described in earlier sections of this thesis, utilizes the mixing power of energetic ions to randomize an existing structure. The relationship between the resulting structure and one which is obtained by liquid quenching or vapor deposition is not clear. Defects and inhomogeneities which are characteristic of the fabrication technique might be produced during the bombardment. In addition remnants of the original structure may

persist due to an incomplete mixing. We have measured the superconducting properties of such films and have found evidence for a very inhomogeneous structure.

In this study samples were prepared by mixing layers of Mo and Ru with 300 keV Xe^+ ions. The overall composition was controlled by varying the relative thickness of the Mo and Ru layers, and was designed to be $Mo_{55}Ru_{45}$. The preirradiated sample consisted of four layers each of Mo and Ru, each about 50-90 Å thick. Samples from the same evaporation were subjected to four irradiation doses which were, 7, 10, 13 and 17 in units of 10^{15} ions/cm^2. The samples will henceforth be referred to as 7, 10, 13 and 17.

Reed camera x-ray diffraction revealed an amorphous band in all cases with occasional evidence for crystalline phases. Transmission electron microscopy revealed very similar structures for all four samples. Fig. 35a shows a representative case. The structure is very inhomogeneous consisting of a grey amorphous matrix with 50-100 Å crystals (light and dark regions) interspersed throughout. A careful examination of the grey amorphous matrix reveals lighter features above ∿10 Å across which may be Xe bubbles. The electron diffraction pattern (35b) consists of broad rings which are a superposition of the amorphous pattern and non-resolved crystalline rings.

Table 6 summarizes the T_c and H_{c_2} data for the four samples. This behavior is complicated by the inhomogeneous nature of these samples. It is not clear which phase (crystalline or amorphous) is dominating the superconducting behavior of the sample.

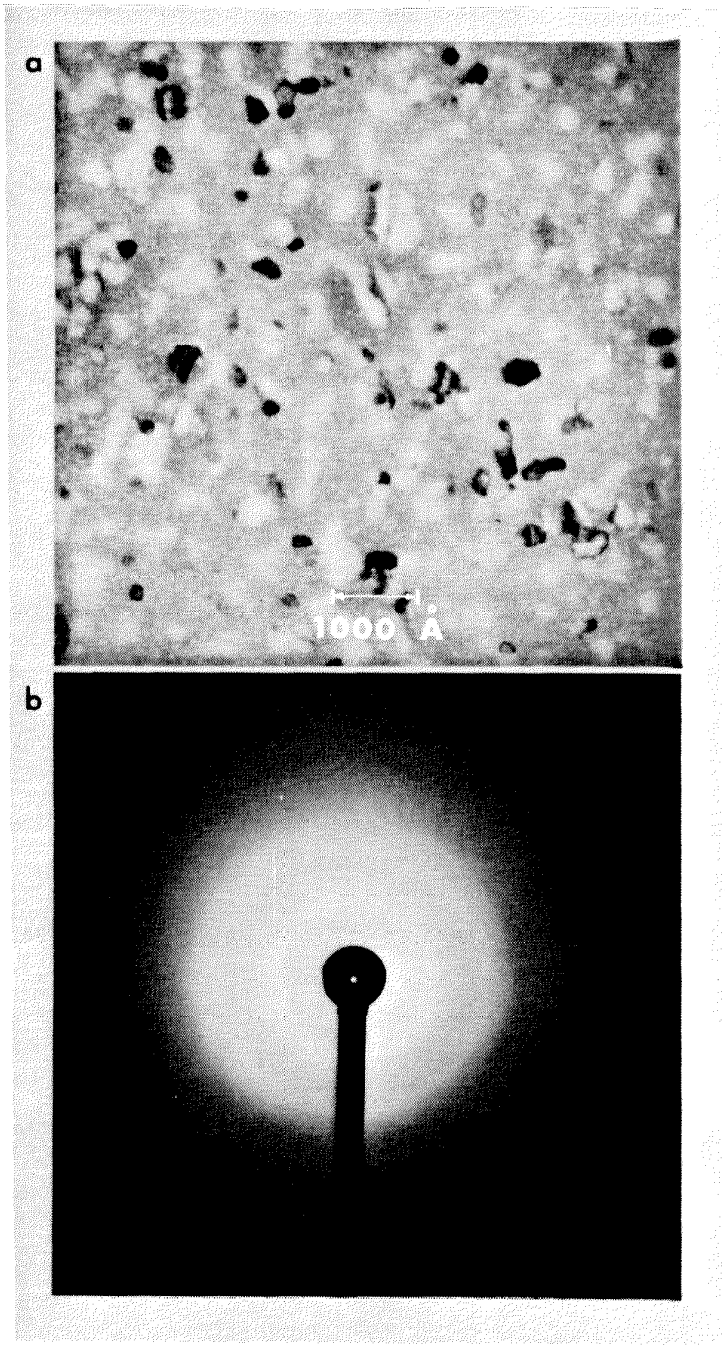

Figure 35. Results of structural analysis of ion beam mixed $Mo_{55}Ru_{45}$ a) electron micrograph b) electron diffraction pattern.

Ion Dose $(\frac{ions}{cm^2})$	$T_c(K)$	$\left.\frac{dH_{c_2}}{dt}\right\|_{T_c}$ $(\frac{kOe}{K})$	$H_{c_{2_R}}(4.2)(kOe)$	$H_{c_{2_P}}(4.2)(kOe)$	$F_{P_m}/H_{c_2}^2$ $(\frac{N}{m^3 Oe^2})$
$7x10^{15}$	7.66	24.1	83.4	67	.111
10^{16}	7.72	22.5	79.2	63	.099
$1.3x10^{16}$	7.42	25.0	80.5	60	.107
$1.7x10^{16}$	7.17	25.4	75.4	59	.124

TABLE 6. Xenon ion dose, transition temperature, critical field gradient, critical field at 4.2K determined from resistive measurements ($H_{c_{2_R}}(4.2)$) and flux pinning measurements ($H_{c_{2_P}}(4.2)$), and flux pinning force parameter for ion beam mixed $Mo_{55}Ru_{45}$ samples.

The result of the flux pinning measurements also reflected the inhomogeneous nature of these samples. The critical currents were the largest of any reported in this thesis with values as high as 1.2×10^4 A/cm^2 at $H = \frac{1}{2}(H_{c_2})$. The value for the critical field at 4.2 ($H_{c_{2_p}}(4,2)$) can be determined by extrapolating flux pinning data to zero current. This value is also given in Table 6. This value is always considerably less than the value determined from H_{c_2} measurements ($H_{c_{2_R}}(4,2)$). The difference between these two numbers is a measurement of the width of the distribution of properties which exist in the sample.

The pinning force parameter $F_p/H_{c_2}^2$ for each of the samples is plotted versus reduced field in Fig. 36. The pinning force profile matches well that from the Larkin-Ovchinikov theory in the strong pinning limit (Fig. 5). The maximum values for the parameter $F_p/H_{c_{2_p}}$ are given in Table 6. The pinning strength decreases then increases as a function of ion dose. The decrease in pinning force from sample 7 to sample 10 is most likely due to the destruction of the remnants of the original crystalline structure. The increase in pinning force following doses greater than 10^{16} ions/cm^2 may be due to either formation of a new crystalline phase or formation of irradiation defects such as Xe gas bubbles. The x-ray diffraction results suggest that σ-MoRu phase is formed at high doses ($>10 \frac{\text{ions}}{\text{cm}^2}$) This is consistent with the decrease in T_c (σ-phase T_c = 7.1 K.[49]) Thus it may be the growth of crystalline inclusions of σ-MoRu which

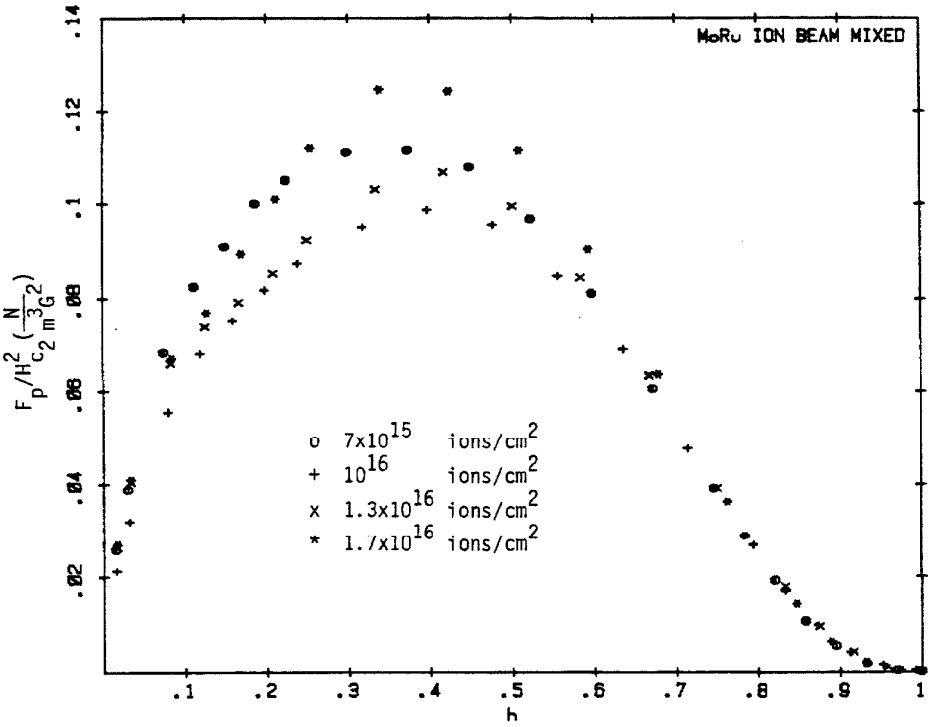

Figure 36. Pinning force parameter $F_p/H_{c_2}^2$ as a function of reduced field for ion beam mixed $Mo_{55}Ru_{45}$. Results are shown for several different irradiation doses.

which is responsible for the increased pinning strength.

In conclusion, the structure which results from the ion beam mixing of alternate layers of Mo and Ru is shown by TEM and superconducting measurements to be very inhomogeneous. The structure consists of an amorphous matrix with 50-100 Å crystalline phase inclusions. TEM also revealed structures resembling Xe gas bubbles. The relationship between the amorphous phase formed in this manner and the amorphous phase formed by liquid quenching or sputter deposition is clouded by the presence of these inclusions. Verification of the presence of Xe bubbles could be achieved by their effect on flux pinning force more easily in purely amorphous materials.

VI. Summary of Results

This thesis has presented the use of superconductivity as a tool to probe the metallurgical state of highly disordered metastable materials. The information gained comes from critical current and critical field measurements. From the results of critical current measurements one can construct a pinning profile which is a plot of pinning force versus field. Thus information comes from the magnitude of the critical current and the shape of the pinning profile. In upper critical field measurements, deviations from the theoretically expected shape of the upper critical field versus temperature curve have been interpreted as evidence for two or more phases existing within the same sample. We have examined materials prepared by three sample fabrication techniques: rapid quenching from the melt, sputter deposition and ion beam mixing.

The critical current measurements performed in liquid quenched materials demonstrated flux pinning by three mechanisms. Crystalline inclusions of σ-MoRu in amorphous $(Mo_{0.6}Ru_{0.4})_{80}Si_{10}B_{10}$ were shown to increase the critical current by about three orders of magnitude over that of the purely amorphous material. The flux pinning profiles for the two cases were very different with the pinning profile for the amorphous plus crystalline inclusion sample being close to the shape of a profile generated by the Larkin-Ovchinnikov collective pinning theory in the strong pinning limit.

In purely amorphous $(Mo_{0.6}Ru_{0.4})_{82}B_{18}$ pinning by surface roughness on the sample edges was found to dominate the critical current characteristics. This effect can be eliminated by appropriate sample geometries and electropolish treatments which allows the relatively weak bulk pinning contribution to dominate. The edge pinning contribution results in a pinning profile similar to those generated by the dynamic pinning model while the main features of the bulk pinning contribution can be duplicated by the Larkin-Ovchinnikov model in the limit of relatively weak pinning.

Thermal annealing of $(Mo_{0.6}Ru_{0.4})_{82}B_{18}$ produced two effects on the pinning strengths. First a decrease occurs which is interpreted as resulting from the annealing out of quenched in inhomogeneous strains or excess volume defects and is correlated with a decrease in T_c. The second effect was an increase in pinning force due to a growth of an inhomogeneity such as decomposition into boron poor and boron rich phases as a precursor to crystallization.

The upper critical field behavior of amorphous $(Mo_{0.6}Ru_{0.4})_{1-x}B_x$ for x = 0.12, 0.18 and 0.22 was studied for samples in the as quenched and annealed condition. The transition width increased following an anneal, reflecting the increased presence of inhomogeneities. Recently it has been suggested that the extended linear region typical of the upper critical field curves in amorphous Mo-based alloys is the result of inhomogeneities. However, we observed that the annealed samples exhibited a greater downward curvature in $H_{c_2}(T)$ curves than the more

homogeneous unannealed samples. This behavior is interpreted as being the result of the superconducting coherence length becoming larger than the spatial dimensions of the high H_{c_2} high T_c regions of the sample.

Superconducting measurements were performed on sputter deposited amorphous $(Mo_{0.6}Ru_{0.4})_{82}B_{18}$ deposited in varying Ar pressures and in the unannealed and annealed condition. Sputter deposition in low Ar pressure (5 μm) produced material which exhibits many of the properties of liquid quenched material. Quenched in strains or excess volume seem to be present to a greater degree than in liquid quenched materials as evidenced by a larger drop in T_c upon annealing. Evidence for phase separation is observed in flux pinning measurements. A peak in the flux pinning profile which occurs in the sputtered material is thought to be attributable to an intrinsic inhomogeneity which occurs in the sputtered materials but not in the liquid quenched materials but may be due to the two-dimensional character of the flux pinning in the thinner sputtered materials. The pinning force follows the 2-d Larkin-Ovchinnikov weak pinning field dependence at low fields (below the peak) and the 2-d Larkin-Ovchinnikov strong pinning field dependence at high fields. Sputter deposition in higher Ar pressure (75 μm) produced very inhomogeneous materials as evidenced by T.E.M., flux pinning profile, and H_{c_2} measurements.

The structure which results from the ion beam mixing of alternate layers of Mo and Ru is shown by TEM and superconducting measurements

to be very inhomogeneous. TEM revealed a structure consisting of an amorphous matrix with 50-100 Å crystalline phase inclusions, and smaller structures resembling Xe gas bubbles. The pinning profiles obtained are characteristic of a strong pinning mechanism and the magnitude of the critical currents are the highest of any of the materials measured for this thesis. The magnitude of flux pinning force first decreased and then increased as a function of ion beam dose. The decrease is attributed to the destruction of remnants of the original structure while the increase is due to the formation of an inhomogeneity such as σ-MoRu crystalline inclusions or Xe gas bubbles. Verification of the presence of Xe bubbles could be achieved by their effect on flux pinning force more easily in purely amorphous materials. The relationship between the amorphous phase formed by ion beam mixing and the amorphous phase formed by liquid quenching or sputter deposition is clouded by the presence of inclusions.

REFERENCES

1. J. M. Ziman, "Models of Disorder", Cambridge University Press (1979).
2. P. W. Anderson, Phys. Rev. 109, 1492 (1958).
3. A. R. Williams, PhD Thesis, Caltech, Pasadena, California, 1981.
4. A. Brenner and G. Riddell, J. Res. Natl. Bur. Stand. 37, 31 (1946).
5. A. Brenner, C. D. Couch and E. Kellog-Williams, J. Res. Natl. Bur. Stand. 44, 109 (1950).
6. W. Buchel and R. Hilsch, Z. Phys. 138, 109 (1954).
7. W. Klement, R. H. Willens, and P. Duwez, Nature 187, 869 (1960).
8. Myron Strongin, O. F. Krammerer, J. E. Crow, R. D. Parks, D. H. Douglas, Jr., and M. A. Jensen, Phys. Rev. Lett. 21, 1320 (1968). M. Strongin, Physica 55, 155 (1971).
9. M. M. Collver and R. H. Hammond, Phys. Rev. Lett. 30, 92 (1973).
10. W. L. Johnson and S. J. Poon, IEEE Trans, on Mag. MAG-11, 189 (1975).
11. H. Kamerlingh Onnes, Leiden Comm. 120b, 122b, 124c (1911).
12. W. Meissner and R. Ochsenfeld, Naturwissenschaften 21, 787 (1933).
13. J. Bardeen, L. N. Cooper, and J. R. Schrieffer, Phys Rev. 108, 1175 (1957).
14. M. Tinkham, "Indroduction to Superconductivity", McGraw Hill Book Co. (1975).
15. G. M. Eliashberg, Zh. Eksp. Teor. Fiz. 38, 966 (1960).
16. W. L. McMillan, Phys. Rev. 167, 331 (1968).
17. W. L. Johnson, in "Glassy Metals I", edited by H. J. Guntherodt and H. Beck (Springer-Verlag, Berlin, 1981), pg. 191.
18. G. Bergmann, Phys. Reports (Sect. C of Phys. Lett.) 27, 159 (1976).
19. C. M. Varma and R. C. Dynes, in "Superconductivity in d- and f-band Metals", edited by D. H. Douglass (Plenum, New York 1976).

20. D. Saint-James, E. J. Thomas, and G. Sarma, "Type II Superconductivity", Pergamon Press, Oxford (1969).

21. L. P. Gorkov, Zh. Eksperim. i Teor. Fiz 36, 1918 (1959) [Soviet Phys.-JETP 9, 1364 (1959)].

22. Kazumi Maki, Physics 1, 21 (1964).

23. E. Helfand and N. R. Werthamer, Phys. Rev. 147, 288 (1966).
N. R. Werthamer, E. Helfand, and P. C. Hohenberg, Phys. Rev. 147, 295 (1966).

24. A. A. Abrikosov, Zh. Eksperim. i Theor. Fiz. 32, 1442 (1957) [Soviet Phys.-JETP 5, 1174 (1957)].

25. Y. B. Kim, C. F. Hempstead, and A. R. Strnad, Phys. Rev. 139, A1163 (1963).

26. E. J. Kramer, J. Appl. Phys. 44, 1360 (1973).
E. J. Kramer, "Proc. of Intl. Disc. Meet. on Flux Pinning in Superconducters", ed. P. Haasen and H. C. Freyhardt, Sonnenberg, Germany (1974), pg. 240.

27. A. M. Campbell and J. E. Evetts, Adv. Phys. 21, 199 (1972).

28. R. P. Huebener, "Magnetic Flux Structures in Superconductors", Springer-Verlag Heidleberg (1979).

29. R. Labusch, Crys. Lat. Defects 1, 1 (1969).

30. K. Yamafuji and F. Irie, Phys. Lett. 25A, 387 (1967).

31. A. I. Larkin and Yu. N. Ovchinnikov, J. Low Temp. Phys. 34, 409 (1979).

32. J. Pearl, J. Appl. Phys. 37, 4139 (1966).

33. E. J. Kramer and A. Das Gupta, Phil. Mag. 26, 769 (1972).

34. A. Das Gupta and E. J. Kramer, Phil. Mag. 26, 779 (1972).

35. E. H. Brandt, Phys. Stat. Sol. (b) 77, 551 (1976).

36. J. W. Christian, "The Theory of Transformation in Metals and Alloys", Pergamon Press, Oxford (1975).

37. Madhav Mehra, (to be published).

38. U. Koster and U. Herold, in "Glassy Metals I", ed. H. J. Guntherodt and H. Beck (Springer-Verlag, Berlin 1981) pg. 225.

39. M. Tenhover, PhD Thesis, Caltech, Pasadena, California (1981).

40. C. O. Kim and W. L. Johnson, Phys. Rev. B 23, 143 (1981).

41. S. T. Hopkins, Solid State Comm. (in press).

42. J. Piller and P. Haasen, Acta Met. 30, 1 (1982).

43. J. W. Cahn, Acta Met. 9, 795 (1961).
J. W. Cahn, Acta Met. 10, 179 (1962).

44. P. Pietrokowsky, Rev. Sci. Instrum. 34, 445 (1963).

45. R.B. Pond, "Metallic Filaments and Method of Making Same", U. S. Patent No. 2,825,108 (1958).

46. D. Raskin, personal communication.

47. K. R. Efferson, Rev. Sci. Instr. 38, 1776 (1967).

48. E. Anderson and W. Hume-Rothery, J. Less Common Met. 2, 443 (1960).

49. E. Bucher, F. Heiniger, and J. Müller, Helv Phys. Acta 34, 843 (1961).

50. G. Deuescher and P. G. de Gennes, "Superconductivity", edited by R. D. Parks (Dekker, New York, 1969) pg. 1005.

51. W. Silvert and A. Singh, Phys. Rev. Lett. 28, 222 (1972).

52. E. R. Domb and W. L. Johnson, J. Low Temp. Phys. 33, 29 (1978).

53. M. Tenhover, W. L. Johnson, and C. C. Tsuei, Solid State Comm. 32, 981 (1979).

54. W. L. Johnson, J. Appl. Phys. 50, 1557 (1979).

55. W. L. Johnson and A. R. Williams, Phys. Rev. B 20, 1640 (1979).

56. R. Schulz, private communication.

57. C. C. Koch, D. M. Kroeger, J. S. Lin, J. O. Scarbrough, W. L. Johnson, and A. C. Anderson, Phys. Rev. B (submitted 1982).

58. A. Drehman and W. L. Johnson, Phys. Stat. Sol. (a) 52,499 (1979).

59. R. Hasegawa, V. R. V. Ramanan, and G. E. Fish, J. Appl. Phys. 53 2276 (1982).

60. J. L. Walter, D. G. LeGrand, and F. E. Luborsky, General Electric Report No. 77CRD011 (1977).

61. K. Osamura, K. Shibue, R. Suzuki, and Y. Marakami, Colloid and Polymer Sci. 259, 667 (1981).

62. J. Kästner, H. R. Löhneysen, M. Platie, and K. Samwer, Proceedings for Conference on Metallic Glasses, Budapest (1980).

63. B. M. Clemens, M. Tenhover, and W. L. Johnson, Physica 107B, 319 (1981).

64. W. L. Carter, S. J. Poon, G. W. Hull, Jr., and T. H. Geballe, Solid State Comm. (in press 1981).

65. S. K. Khanna, A. P. Thakoor, R. F. Landel, Madhav Mehra, and W. L. Johnson, Appl. Phys. Comm. (submitted 1982).

66. A. M. Flank, M. Harmelin, M. Jaulin, and A. Naudon, Revue Phys. Appl. 15, 1427 (1980).

67. M. G. Scott and R. Maddin,"Proc. 2nd Intl. Conf. Rapidly Quenched Metals" 1, 249 (1976).

68. B. Schroeder, W. L. Johnson, C. C. Tsuei, and P. Chaudhari, "Structure and Excitations in Amorphous Solids", AIP Conference Proceedings No. 31, 353 (1976).

69. P. H. Kes and C. C. Tsuei, Phys. Rev. Lett. 47, 1930 (1981).

70. D. L. Whiting, Senior Thesis, Caltech, Pasadena, California (1980).

71. A. Davidson and M. Tinkham, Phys. Rev. B 13, 3261 (1976).

72. Madhav Mehra (personal communication 1982).

73. R. B. Laibowitz, E. I. Alessandrini, and G. Deutscher, I.B.M. Research Report No. RC 9155 (#40079) (1981).

74. W. A. Grant, A. Ali, L. T. Chadderton, P. G. Grundy, and E. Johnson, "Proc. 3rd Int. Conf. on Rapidly Quenched Metals" 1, 63 (1978).